Reconstruction subgrid models for nonpremixed combustion

J. P. Mellado and S. Sarkar[a)]
Department of Mechanical and Aerospace Engineering, University of California–San Diego, La Jolla, California 92093-0411

C. Pantano
Graduate Aeronautical Laboratories, California Institute of Technology, M/C 205-45, Pasadena, California 91125

(Received 31 January 2003; accepted 17 July 2003; published 16 September 2003)

Large-eddy simulation of combustion problems involves highly nonlinear terms that, when filtered, result in a contribution from subgrid fluctuations of scalars, Z, to the dynamics of the filtered value. This subgrid contribution requires modeling. Reconstruction models try to recover as much information as possible from the resolved field $\bar{Z}$, based on a deconvolution procedure to obtain an intermediate field Z_M. The approximate reconstruction using moments (ARM) method combines approximate reconstruction, a purely mathematical procedure, with additional physics-based information required to match specific scalar moments, in the simplest case, the Reynolds-averaged value of the subgrid variance. Here, results from the analysis of the ARM model in the case of a spatially evolving turbulent plane jet are presented. *A priori* and *a posteriori* evaluations using data from direct numerical simulation are carried out. The nonlinearities considered are representative of reacting flows: power functions, the dependence of the density on the mixture fraction (relevant for conserved scalar approaches) and the Arrhenius nonlinearity (very localized in Z space). Comparisons are made against the more popular beta probability density function (PDF) approach in the *a priori* analysis, trying to define ranges of validity for each approach. The results show that the ARM model is able to capture the subgrid part of the variance accurately over a wide range of filter sizes and performs well for the different nonlinearities, giving uniformly better predictions than the beta PDF for the polynomial case. In the case of the density and Arrhenius nonlinearities, the relative performance of the ARM and traditional PDF approaches depends on the size of the subgrid variance with respect to a characteristic scale of each function. Furthermore, the sources of error associated with the ARM method are considered and analytical bounds on that error are obtained. [DOI: 10.1063/1.1608008]

I. INTRODUCTION

Turbulent combustion involves a wide range of spatio-temporal scales and requires a large number of dependent variables (e.g., species mass fractions), two facts that make direct numerical simulation (DNS) of realistic cases impossible with current computational resources. Models are required and considerable effort has been devoted to the subject.[1–5]

Classical moment-based methods pose many difficulties due to the strong nonlinear character of the reaction terms. Besides, the turbulent transport terms are not well represented by the gradient transport models used with passive scalars.[4] A different general approach consists of writing the problem in terms of the one-point probability density function (PDF)[6,7] and trying to solve the corresponding transport equation. The reaction terms are now closed, but closure is required for the pressure and molecular mixing terms. Active research is being done in this framework, working with reduced mechanisms and modeling the transport equation for the joint PDF of the corresponding scalars.[8]

A popular formulation in nonpremixed turbulent combustion tries to take advantage of the conserved scalars that might appear in the problem. If it is possible to derive state relations of the form $\psi_i = \psi_i(Z)$, where ψ_i represents the reactive scalars and Z a conserved scalar, then the knowledge of information about Z provides information about ψ_i.[2,4,9,10] The relations $\psi_i(Z)$ are derived using the fact that chemical times, t_c, are very often small compared to flow times, t_f, and hence the Damköhler number, $\mathrm{Da} = t_f/t_c$, is large. Two final simplifying assumptions can then be made: either to consider reversible infinitely fast chemistry, having the equilibrium composition at each point in space and instant of time, or to consider irreversible infinitely fast chemistry with an overall single-step chemical reaction model, the so-called Burke–Schumann solution, which leads to a flame sheet representation.

The flame sheet approach suggested the view of nonpremixed turbulent reacting flows as an ensemble of laminar thin one-dimensional diffusive-reactive layers, called flamelets, embedded in an otherwise nonreactive turbulent flow.[11] This concept leads to equations for ψ_i in terms of the mixture fraction Z, with the scalar dissipation rate χ as a parameter.[4,12–14] Solution of this set of equations gives ψ_i

a)Author to whom correspondence should be addressed. Telephone: (858) 534 8243; fax: (858) 534 7599. Electronic mail: ssarkar@mae.ucsd.edu

$=\psi_i(Z;\chi_{st})$, and if the joint PDF of Z and χ_{st} is assumed, statistical information about species mass fractions and temperature is known.

Recently, the conditional moment closure approach has been proposed as an alternative to flamelet models.[15,16] Instead of taking the usual (unconditional) average of the scalars, the expectation is taken conditional to the mixture fraction being a defined value, and transport equations are derived for these conditional moments, equations that require again closure for certain terms. Similarities and differences with the flamelet model are currently a topic of research.[4,17]

During the past decade, large-eddy simulation (LES) has increasingly been used for modeling nonpremixed turbulent combustion, given its relative success in nonreacting turbulent flows. The present work falls into this category. In LES, the problem is formulated in terms of the filtered variables, and filtering the governing equations brings into the problem subgrid-scale (SGS) contributions to the dynamics of the resolved fields from the subgrid (subfilter, unresolved) scales; these contributions are unknown and have to be modeled. Each nonlinear term causes a subfilter counterpart, and these nonlinear terms appear either in the direct approach (e.g., through the chemical production terms in the species conservation equations) or in the conserved scalar approach [e.g., the state relations $\psi_i(Z)$]. The resolved field, $\overline{Z}(\mathbf{x},t)$, is given by the LES and therefore the resolved part of the nonlinear term, $f(\overline{Z})$, is known. The question is what is the subgrid contribution

$$f(Z)_{\mathrm{sg}}(\mathbf{x},t)=\overline{f(Z)}-f(\overline{Z}), \tag{1}$$

to the total term $\overline{f(Z)}$. The filtering operation of a variable ϕ is denoted by $\overline{\phi}$. Z will be thought of as a conserved scalar, like a mixture fraction, ranging from 0 to 1, but nothing prevents the results to be applied to a nonconserved quantity, like a species mass fraction.

One possible approach to model scalar mixing in LES is the linear-eddy model.[18] Applications to combustion problems have been reported in the literature[19,20] Another type of approach is based on PDFs. In this method, the filtering operation is written in terms of the filtered (subgrid-scale, large-eddy) PDF, which describes the stochastic behavior of the scalar, Z, inside the grid cell. One solution is to model the transport equation for this PDF.[21,22] However, the most popular procedure is to presume certain distribution, generally a beta PDF.[23,24] This latter procedure requires two inputs: the filtered field $\overline{Z}$, available directly from a LES, and the subgrid variance,

$$Z^2_{\mathrm{sg}}(\mathbf{x},t)=\overline{Z^2}-\overline{Z}^2, \tag{2}$$

not available directly and, therefore, in need of modeling [for notational convenience, the subgrid-scale variance will be generally denoted by Z^2_{sg}, instead of the more correct notation, $(Z^2)_{\mathrm{sg}}$; this latter representation will be used when confusion with $(Z_{\mathrm{sg}})^2$ might arise]. The scale similarity approach[24] with the coefficient calculated using an assumed scalar spectrum,[25] and the gradient model[26] are two possibilities to estimate the subfilter variance. *A priori* tests of the beta PDF model have been performed in previous studies using direct numerical simulation (DNS) data, for example, isotropic turbulence with equilibrium chemistry and no heat release,[24] isotropic turbulence with a flamelet model and no heat release[27] and isotropic turbulence with a flamelet model and heat release.[28] Further *a priori* analysis has been carried out for a shear layer with infinitely fast chemistry and no heat release,[29] and a round jet with finite-rate chemistry and heat release.[30] An overall conclusion of the *a priori* studies is that the beta-PDF model gives good predictions if the *exact pointwise* subfilter scalar variance is available. Some *a posteriori* studies have been performed, for example, a turbulent round jet of nonpremixed methane–air with a pilot.[31]

Approximate reconstruction using moments (ARM) model[32] is an alternative approach that avoids the intermediate step of modeling the PDF of the subgrid-scale fluctuation. Similar to other reconstruction models, it recovers information from the filtered field, $\overline{Z}(\mathbf{x},t)$. However, in addition, the *average* value of the subfilter scalar variance, obtained for example from the ''small scale'' behavior of the scalar spectrum, is provided. In its simplest version, it is based on the filter size, Δ_f, and physical quantities, namely, expected values of the turbulent kinetic energy, K, the scalar variance, Z^2_{rms}, and the scalar dissipation, $\chi=\langle 2D\nabla Z\cdot\nabla Z\rangle$, which can be reasonably estimated from a LES (though χ is often used for the instantaneous value in combustion literature, here it is chosen to represent the expected value for notational convenience). As a special case, the ARM model can be used to estimate the subgrid variance required in the PDF approach.

In the present work, reconstruction models are discussed for a single-scalar nonlinear function, with particular emphasis on the ARM model. After describing different aspects of these approaches, *a priori* and *a posteriori* analysis of the ARM model in a spatially evolving turbulent plane jet are presented. The sources of error in the ARM procedure are then analyzed. The discussion is concluded presenting comparisons with the assumed PDF approach.

II. RECONSTRUCTION SUBGRID-SCALE MODELS

Let $Z(\mathbf{x},t)$ be a scalar field defined over Ω, the volume occupied by the flow variables, at a certain time t. The filtering operation is a linear transformation between two function spaces, say $\mathcal{G}:L^2(\Omega)\rightarrow L^2(\Omega)$, defined by

$$\overline{Z}(\mathbf{x},t)=\mathcal{G}Z(\mathbf{x},t)=\int_{\Omega}G(\mathbf{x},\mathbf{r})Z(\mathbf{r},t)\,d\mathbf{r}. \tag{3}$$

Time, t, enters only as a parameter and will not be shown explicitly in the following discussion. If the filter is homogeneous, i.e., $G(\mathbf{x},\mathbf{r})=G(\mathbf{x}-\mathbf{r})$, then the filtering operation is reduced to a convolution in physical space between the field $Z(\mathbf{x})$ and the filter kernel $G(\mathbf{x})$.[33]

Reconstruction subgrid-scale models try to recover as much information as possible from $\overline{Z}(\mathbf{x})$ at each instant of time. If the operator $\mathcal{G}$ admits an inverse, then the complete original field $Z(\mathbf{x})$ can be recovered. However, the filters used in LES are not invertible, and, at most, only part of the original field is recovered. This reconstruction provides an

intermediate scalar $Z_M(\mathbf{x})$, which is used to compute either the subgrid-scale part or the total part of the nonlinearity $f(Z)$ according to Eq. (1).

The first reconstruction approach was the *scale similarity model* (SSM),[34] which improved considerably the correlation between model and exact subgrid-scale fields compared to the typical gradient-based approach. The *subgrid-scale estimation model*[35,36] involves a deconvolution step on the LES field (Δ_f resolution) followed by the introduction of a finer mesh ($\Delta_f/2$ resolution) to allow the representation of the nonlinear contribution, $\mathbf{u}\cdot\nabla\mathbf{u}$, from scales between Δ_f and $\Delta_f/2$. More recently, the *approximate deconvolution model* (ADM)[37,38] has been introduced to estimate the unfiltered field by a truncated series expansion of the ''inverse filter operator.'' Finally, the *approximate reconstruction using moments* (ARM) model[32] modifies this last approach to bring certain physical information into the pure mathematical procedure of deconvolution.

A. Deconvolution operation

A sufficient (not necessary) condition for a linear operator $\mathcal{G}$ to have a bounded inverse $\mathcal{G}^{-1}$ is $\|\mathcal{I}-\mathcal{G}\|<1$, in which case $\mathcal{G}^{-1}$ can be represented by the *Neumann series*

$$\mathcal{Q}=\sum_{n=0}^{\infty}(\mathcal{I}-\mathcal{G})^n. \tag{4}$$

Linear operator theory provides more general conditions for the existence of the inverse operator,[39,40] but this result is sufficient for the following discussion. The problem is that $\mathcal{G}^{-1}$ exists if and only if the null space of $\mathcal{G}$, $N(\mathcal{G})$, contains only the zero function, and that is not the case in LES. Using Fourier analysis and denoting the Fourier transform of any variable ϕ by $\hat{\phi}$,

$$\hat{\phi}(\boldsymbol{\kappa})=\frac{1}{(2\pi)^3}\int_{\mathbb{R}^3}\phi(\mathbf{x})e^{-i\boldsymbol{\kappa}\cdot\mathbf{x}}\,d\mathbf{x}, \tag{5}$$

the null space of $\mathcal{G}$ is given by $\hat{G}\hat{Z}=0$, which corresponds to the zeros of the filter transfer function $\hat{G}(\boldsymbol{\kappa})$ for $\hat{Z}\neq 0$. From a theoretical standpoint, a *Gaussian filter* can be inverted because its filter transfer function does not have any zero. Similarly, the null space of the *top-hat filter* is a set of zero measure, with the only effect of eliminating particular frequencies but without repercussion on the final energy of the field. For a *sharp spectral cutoff filter*, information beyond the cutoff frequency is unrecoverable. The representation of $Z(\mathbf{x})$ on a discrete grid in physical space implicitly imposes a spectral cutoff, and therefore, in the discrete case, nothing can be recovered from wavelengths smaller than $2\Delta_g$, where Δ_g denotes the grid spacing. Thus, in LES applications, $\mathcal{G}^{-1}$ does not formally exist.

This fact suggests to decompose the field $Z(\mathbf{x})$ as

$$Z=\overline{Z}+Z_{\mathrm{sg}}=\overline{Z}+Z_{\mathrm{sg},r}+Z_{\mathrm{sg},u}, \tag{6}$$

where the subgrid term has been split into a *recoverable part*, $Z_{\mathrm{sg},r}$, and an *unrecoverable part*, $Z_{\mathrm{sg},u}$. The former one is defined by

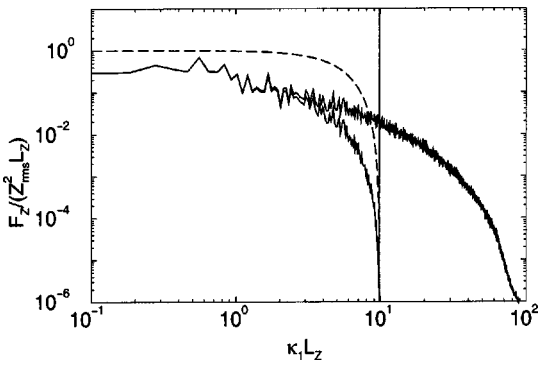

FIG. 1. One-dimensional spectrum of Z (upper solid curve) and $\overline{Z}$ (lower solid curve) obtained from DNS. Dashed line indicates $\hat{G}^2$ of the top-hat filter plus the spectral cutoff (vertical solid line) introduced by the LES grid, $\Delta_g=\Delta_f/2$.

$$Z-Z_{\mathrm{sg},u}=\overline{Z}+Z_{\mathrm{sg},r}=\mathcal{Q}\overline{Z} \tag{7}$$

and the latter needs modeling. Figure 1 shows an example of the spectra (power spectral densities) of Z and $\overline{Z}$ using a top-hat filter. The difference between these two spectra represents the energy in the subgrid scales. To the left of the vertical line, which denotes the position of the filter in wave number space, the scales are recoverable by the LES grid and to the right they are not. Hence, the deconvolution operation is useful for cases in which the filter is not a sharp spectral cutoff because it allows us to recover information of scales close to the filter size Δ_f.

The justification for the effort in recovering the subgrid scales $Z_{\mathrm{sg},r}$ lies in how much of the whole subgrid field is represented by them. To clarify this point we proceed to estimate the expected value of the subfilter variance. The expected value (Reynolds-averaged value) of any variable ϕ is denoted by $\langle\phi\rangle$. In an isotropic case, we can use Fourier analysis and work in wave number space to obtain[41]

$$\langle\overline{Z^2}-\overline{Z}^2\rangle=\langle Z^2-\overline{Z}^2\rangle=\int_0^{\infty}(1-\hat{G}^2)E_Z\,d\kappa, \tag{8}$$

where $E_Z(\kappa)$ is the three-dimensional scalar spectrum and $\hat{G}(\kappa)$ is the filter transfer function [multiplied by $(2\pi)^3$]. Note that interchanging the Reynolds average and the filter (both are linear operations) gives $\langle\overline{Z^2}\rangle=\overline{\langle Z^2\rangle}$ and, assuming homogeneity, $\langle Z^2\rangle$ is constant, yielding $\overline{\langle Z^2\rangle}=\langle Z^2\rangle$. All the discussion will be presented for a top-hat filter, for which

$$\hat{G}(\kappa)=\sin\xi/\xi, \tag{9}$$

where $\xi=\gamma\kappa L_Z$ and γ is defined by

$$\gamma=\Delta_f/2L_Z. \tag{10}$$

Other filters in physical space were considered and the corresponding results are shown in Appendix A, where it is observed that there are little differences among them. In these expressions Δ_f is the filter size and $L_Z=K^{1/2}Z_{\mathrm{rms}}^2/\chi$ is a large scale of the scalar fluctuations. The turbulent kinetic energy is denoted by K and χ represents the expected value of the scalar dissipation. If we assume that the nonzero re-

gion of $(1-\hat{G}^2)$ in Eq. (8) occurs for wave numbers well into the inertial range we can then adopt the Obukhov–Corrsin spectrum,[42]

$$E_Z(\kappa)=C_c\epsilon^{-1/3}\chi\kappa^{-5/3}, \tag{11}$$

ϵ being the turbulent kinetic energy dissipation, which yields

$$\langle Z_{\rm sg}^2\rangle/(Z_{\rm rms}^2 C_c\gamma^{2/3})=\int_0^\infty (1-(\sin\xi/\xi)^2)\xi^{-5/3}\,d\xi$$
$$=1.4352. \tag{12}$$

Equation (12) is important because it relates the filter size Δ_f, embedded in γ, with the level of subfilter fluctuations. On the other hand, the filter size corresponds to $\xi=\pi$ and therefore the amount of subgrid-scale energy recoverable by reconstruction is the above integral over the interval $\xi\in[0,\pi]$, which yields 0.7433. These figures indicate that, if the assumptions made hitherto hold, the percentage of subgrid-scale energy reconstructible in the case of a top-hat filter is about 50%, *independent* of the filter size, as long as the subgrid scales are well inside the inertial subrange. This simplified analysis helps to explain why deconvolution procedures have proved to yield good results.[37,38]

A second consideration is that, for practical applications, the series defining $\mathcal{Q}$ has to be truncated at a certain order, having finally an operator $\mathcal{Q}_M$ that provides the intermediate field $Z_M(\mathbf{x})$,

$$Z_M=\mathcal{Q}_M\overline{Z}. \tag{13}$$

Writing it explicitly,

$$Z_M=\overline{Z}+(\overline{Z}-\bar{\bar{Z}})+(\overline{Z}-2\bar{\bar{Z}}+\bar{\bar{\bar{Z}}})+\cdots. \tag{14}$$

The rate of convergence of the series, Eq. (14), is of similar importance to convergence itself, since each term in the expansion involves an additional filtering operation and the deconvolution procedure can become computationally too expensive. It turns out that the series in Eq. (14) converges slowly for turbulent scalar fields $Z(\mathbf{x})$. *A priori* analysis of the deconvolution procedure using DNS of a temporal mixing layer[32] showed that five terms in the expansion were required to recover peaks of the expected value $\langle Z_{\rm sg}^2\rangle$, the subgrid contribution to $\langle\overline{Z^2}\rangle$, to about 90% (depending on the filter size). A way to avoid this shortcoming is to redefine a new inversion kernel, shorter than the series in Eq. (14), such that certain information about the original field is recovered.[37]

Thus, the deconvolution procedure has two drawbacks. First, information about wavelengths smaller than the LES grid cutoff is unrecoverable. Second, the series in Eq. (14) exhibits slow convergence to the recoverable part of the field. The deconvolution approach is only a mathematical technique, and it does not account for the missing subfilter part of the spectrum. The fact that the field $Z(\mathbf{x})$, at a certain time t, is a solution of the Navier–Stokes equations has not been used. The ARM model[32] is a modification of the reconstruction that involves certain physics of these small scales.

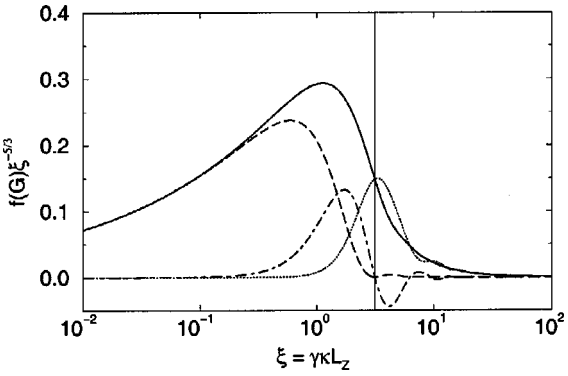

FIG. 2. Contribution to the total subgrid-scale variance (solid line) by the different terms: – – –, Leonard part; – – –, cross part; and ···, Reynolds part. The vertical solid line indicates filter position, $\xi=\pi$.

This allows us to decrease the cost of an approximate reconstruction and, more importantly, to include a compensation for the unresolved subgrid scales.

B. Deconvolution and the scale-similarity model

It is interesting to compare the idea of reconstruction with the traditional scale-similarity model. Decomposing the scalar field into a filtered value and a small-scale fluctuation by $Z=\overline{Z}+Z_{\rm sg}$, the subgrid variance becomes

$$(Z^2)_{\rm sg}=\underbrace{\overline{\bar{Z}^2}-\bar{\bar{Z}}^2}_{\mathcal{L}^0}+\underbrace{2(\overline{\bar{Z}Z_{\rm sg}}-\bar{\bar{Z}}\,\overline{Z_{\rm sg}})}_{\mathcal{C}^0}+\underbrace{\overline{Z_{\rm sg}^2}-\overline{Z_{\rm sg}}^2}_{\mathcal{R}^0}, \tag{15}$$

where the different terms $\mathcal{L}^0$, $\mathcal{C}^0$, and $\mathcal{R}^0$ are the *generalized Leonard part*, *cross part*, and *Reynolds part*, respectively. We use the symbol $(Z^2)_{\rm sg}$ for the subgrid-scale variance $Z_{\rm sg}^2$ for clarity in notation, not to be confused with $(Z_{\rm sg})^2$. In order to determine the relative importance among these components, the Obukhov–Corrsin spectrum is used to estimate their expected value,

$$\langle\mathcal{L}^0\rangle/(Z_{\rm rms}^2C_c\gamma^{2/3})=\int_0^\infty(1-\hat{G}^2)\hat{G}^2\xi^{-5/3}\,d\xi=0.3596,$$
$$\langle\mathcal{C}^0\rangle/(Z_{\rm rms}^2C_c\gamma^{2/3})=\int_0^\infty 2(1-\hat{G}^2)\hat{G}(1-\hat{G})\xi^{-5/3}\,d\xi$$
$$=0.1470, \tag{16}$$
$$\langle\mathcal{R}^0\rangle/(Z_{\rm rms}^2C_c\gamma^{2/3})=\int_0^\infty(1-\hat{G}^2)(1-\hat{G})^2\xi^{-5/3}\,d\xi$$
$$=0.9286,$$

where, as before, $\gamma=\Delta_f/2L_Z$. The integrands of these expressions, which show the contribution of each wave number to the average of the three subgrid-scale terms, are plotted in Fig. 2. The value of the integrals given in Eq. (16) show that 25% of the subgrid energy resides in the Leonard part, 10% in the cross part and 65% in the Reynolds part (note that the abscissas axis is in logarithmic scale). That same graph shows that the energy in the Leonard part and a large amount of the cross part can be reconstructed, along with a small

quantity of the Reynolds term, so that 50% of the subgrid-scale energy is recoverable. Nevertheless, it has to be noted that these percentages only concern the *energy* content, and they say very little about the actual instantaneous representation of the subfilter variance field.

The scale similarity model approximates the subgrid-scale variance by

$$Z_{\mathrm{sg}}^2 \approx \overline{\overline{Z}^2} - \overline{\overline{Z}}^2, \tag{17}$$

that is, only with the Leonard term, which is equivalent to approximate reconstruction with

$$Z_M = \overline{Z}. \tag{18}$$

Hence, the scale similarity model can be interpreted as the leading order term in the deconvolution expansion given by Eq. (14). This only represents about one-fourth of the total subgrid energy according to the previous estimates, and modifications of Eq. (17) have been used to compensate this deficit so that the scale similarity model is given by

$$Z_{\mathrm{sg}}^2 = c(\widetilde{\overline{Z}^2} - \widetilde{\overline{Z}}^2), \tag{19}$$

where the second filter denoted by the tilde is often taken to be larger than the first one and c is a coefficient to be determined. From this point of view, reconstruction can be thought of as a generalized scale similarity model, where higher order terms of the deconvolution expansion have been retained. Thus, it is logical to expect better correlation between exact and model-predicted values of the subgrid-scale variance in the reconstruction procedure with respect to the scale similarity one, as it is confirmed later in the *a priori* analysis.

C. Approximate reconstruction using moments

From the previous discussions, it is clear that the original field cannot be recovered because of the spectral cutoff imposed by the LES grid at $\kappa = \pi/\Delta_g$, where Δ_g is at most $\Delta_f/2$ in order to resolve all the scales down to the filter size. This is the only effect of the numerical part of the LES problem that is retained in this work. The issue of the corruption of the small scales in a simulation due to aliasing and due to the truncation error of the particular numerical scheme chosen should not be forgotten, but the present analysis concentrates only on the analytical part of the problem. The analysis produces certain models and equations, and these should then be solved as exactly as possible: using spectral methods with dealiasing, utilizing high-order compact schemes if inhomogeneous directions are present, and/or ultimately working with a resolution higher than $\Delta_g = \Delta_f/2$.

Since the recovery of the original field $Z(\mathbf{x})$ at each instant of time is impossible, reconstruction methods, though originally motivated by deconvolution, should be understood as trying to find an *intermediate* field $Z_M(\mathbf{x})$ with a different range of scales (namely, only scales larger than Δ_f), such that the field $\overline{f(Z)}(\mathbf{x})$, which is defined on that same range of scales, is well approximated by $\overline{f(Z_M)}(\mathbf{x})$ according to certain criteria. The difficulty is to state clearly those criteria and obtain accordingly an expression for $Z_M(\mathbf{x})$. This is the intent of the ARM model.

1. Subfilter variance Z_{sg}^2

The ARM model introduces the one-parameter family of intermediate fields $Z_M(\mathbf{x})$ given by

$$Z_M = \overline{Z} + c_0(\overline{Z} - \overline{\overline{Z}}), \tag{20}$$

where c_0 is the model coefficient. It is emphasized that Z_M is *not* an approximation to the original field Z, but an intermediate field chosen so as to obtain subgrid contributions to the filtered value $\overline{f(Z)}$. Depending on the closure condition imposed to obtain it, we will get different particular members of the family. Physically, ARM relies on the smallest resolved scales,

$$\overline{Z_{\mathrm{sg}}} = \overline{Z} - \overline{\overline{Z}}, \tag{21}$$

the known small-scale component of the filtered scalar field $\overline{Z}(\mathbf{x})$, of size comparable to Δ_f, to describe the effect of the whole range of subfilter scales. The model coefficient is the amplitude of this field.

In the procedure of approximate reconstruction using moments, the coefficient is calculated so as to match specific subgrid moments of the scalar field, $\overline{Z^n} - \overline{Z}^n$. The first moment is zero, and the second one leads to the closure condition on the subgrid-scale variance,

$$\langle \overline{Z_M^2} - \overline{Z}_M^2 \rangle = \langle \overline{Z^2} - \overline{Z}^2 \rangle. \tag{22}$$

If it were just an approximate reconstruction, this equality of subgrid-scale energy between the two different fields Z and Z_M should be up to the grid cutoff wavelength. ARM goes further by including the energy of the whole subgrid-scale Reynolds part in the intermediate field Z_M through the smallest resolved scales.

Substituting Eq. (20) into Eq. (22) gives the following quadratic equation for c_0:

$$a_2 c_0^2 + a_1 c_0 + a_0 = 0, \tag{23}$$

where

$$\begin{aligned} a_0 &= \langle \overline{\overline{Z}^2} - \overline{\overline{Z}}^2 \rangle - \langle (Z^2)_{\mathrm{sg}} \rangle, \\ a_1 &= 2\langle \overline{\overline{Z}\,\overline{Z_{\mathrm{sg}}}} - \overline{\overline{Z}}\,\overline{\overline{Z_{\mathrm{sg}}}} \rangle, \\ a_2 &= \langle \overline{\overline{Z_{\mathrm{sg}}}^2} - \overline{\overline{Z_{\mathrm{sg}}}}^2 \rangle. \end{aligned} \tag{24}$$

In Eq. (24), the only unknown is $\langle (Z^2)_{\mathrm{sg}} \rangle$. The physical meaning of each coefficient can be seen by writing the generalized decomposition of the subfilter variance, Eq. (15), applied to the intermediate field Z_M,

$$(Z_M^2)_{\mathrm{sg}} = \overline{Z^2} - \overline{\overline{Z}}^2 + 2c_0(\overline{\overline{Z}\,\overline{Z_{\mathrm{sg}}}} - \overline{\overline{Z}}\,\overline{\overline{Z_{\mathrm{sg}}}}) + c_0^2(\overline{\overline{Z_{\mathrm{sg}}}^2} - \overline{\overline{Z_{\mathrm{sg}}}}^2). \tag{25}$$

ARM modifies the energy contained in the resolved cross and Reynolds terms to account for the unresolved part. It is observed as well that the condition $c_0 > 0$ should be imposed to maintain the sign of the contribution from the cross term

equal to that of the original field $Z(\mathbf{x})$ (pointwise correlation results between exact and modeled subfilter variance fields confirm this choice[32]).

The input of the model is the *expected* value $\langle (Z^2)_{\mathrm{sg}} \rangle$, with which Eq. (23) can be solved for c_0. Some additional hypothesis have to be done to estimate the expected value of the subfilter variance, and the model coefficient will deviate from the exact one, that given with the exact $\langle (Z^2)_{\mathrm{sg}} \rangle$ (e.g., from DNS in *a priori* analysis). Therefore, it is interesting to know the sensitivity of the modeled subgrid-scale variance to the model coefficient. This sensitivity is expressed mathematically by

$$\Gamma = \frac{1}{\langle (Z_M^2)_{\mathrm{sg}} \rangle} \frac{\partial \langle (Z_M^2)_{\mathrm{sg}} \rangle}{\partial c_0}, \tag{26}$$

such that the relative error in the prediction of the subgrid-scale variance due to small errors in the model coefficient is just $\Gamma \Delta c_0$. From Eq. (20) we obtain

$$\Gamma = \frac{2a_2 c_0 + a_1}{\langle (Z_M^2)_{\mathrm{sg}} \rangle}. \tag{27}$$

2. General nonlinearity f(Z)

The correct prediction of the subfilter variance is the first part of the ARM model. The second proposition is to compute the subgrid-scale part, $f(Z)_{\mathrm{sg}}(\mathbf{x})$, of a general nonlinearity $f(Z)$ by

$$f(Z)_{\mathrm{sg}} = \overline{f(Z)} - f(\overline{Z}) \approx \overline{f(Z_M)} - f(\overline{Z_M}). \tag{28}$$

The intermediate field is used in the subgrid-scale part of $f(Z)$, instead of the alternative[38] of obtaining the total term. This approach satisfies certain consistency properties, for example, that the invariance of the exact subgrid variance under translation is maintained by Eq. (28), which yields better pointwise behavior.[32]

Analysis of this model for $f(Z)_{\mathrm{sg}}(\mathbf{x})$ is now presented. Consider $Z(\mathbf{r})$ and $f(Z)(\mathbf{r}) = f(Z(\mathbf{r}))$ defined inside the filter cell $\Omega_f(\mathbf{x})$ around a fixed node $\mathbf{x}$ of the LES grid. The Taylor expansion of $f(Z)$ around the fixed value $Z_0 = \overline{Z}(\mathbf{x})$, a constant function in that cell, yields the following formula:

$$f(Z) - f(\overline{Z}) = f'(\overline{Z})(Z - \overline{Z}) + \tfrac{1}{2} f''(\overline{Z})(Z - \overline{Z})^2 + E_2, \tag{29}$$

where the remainder, $E_2(\mathbf{r})$, is given by

$$E_2(\mathbf{r}) = \tfrac{1}{6} f'''(\overline{Z} + \theta(Z - \overline{Z}))(Z - \overline{Z})^3, \tag{30}$$

and $\theta(\mathbf{r})$ has a value between 0 and 1. We are assuming the function $f(Z)$ to be $\mathcal{C}^2$ for $Z \in [0,1]$ and $f'''(Z)$ to exist in (0,1). After filtering the above expression we obtain

$$\overline{f(Z)} - f(\overline{Z}) \approx \tfrac{1}{2} f''(\overline{Z})(\overline{Z^2} - \overline{Z}^2). \tag{31}$$

Equation (31) is an accurate approximation if the *local subfilter fluctuation*,

$$Z_{l\mathrm{sg}}(\mathbf{r}) = Z(\mathbf{r}) - \overline{Z}(\mathbf{x}), \tag{32}$$

is small enough so that E_2 can be neglected. In this case, the same formula can be applied to $f(Z_M)$,

$$\overline{f(Z_M)} - f(\overline{Z_M}) \approx \tfrac{1}{2} f''(\overline{Z_M})(\overline{Z_M^2} - \overline{Z_M}^2), \tag{33}$$

because of the matching in the subfilter variance used by the ARM model to close the subgrid-scale problem, Eq. (22). Therefore,

$$Z_{M,\mathrm{sg}}^2 \approx Z_{\mathrm{sg}}^2 \Rightarrow f(Z_M)_{\mathrm{sg}} \approx f(Z)_{\mathrm{sg}}. \tag{34}$$

Equation (29) does not assume that filtered variables are constant inside the filter cell, $\Omega_f(\mathbf{x})$, but only that the expansion is done about the constant value $f(\overline{Z})$.

Finally, an estimate of the error of the ARM model in predicting $f(Z)_{\mathrm{sg}}(\mathbf{x})$ is given by the filtered value of the remainder in Eq. (29) by taking $\theta = 0$, which yields

$$\begin{aligned} E(\mathbf{x}) &= \frac{f'''(\overline{Z_M})}{3!} \overline{(Z_M - \overline{Z_M})^3} \\ &= \frac{f'''(\overline{Z_M})}{3!} ((Z_M^3)_{\mathrm{sg}} - 3\overline{Z}(Z_M^2)_{\mathrm{sg}}). \end{aligned} \tag{35}$$

In order to quantify the magnitude of the local subfilter field, we use the L^2 norm, $\|\phi\|$, defined with the filter kernel $G(\mathbf{x},\mathbf{r})$ as weighting function by Eq. (A2). The motivation and consequences of this choice of norm are presented in Appendix A, where the local analysis of the filter is described, the main result being

$$\|Z_{l\mathrm{sg}}\| = (Z_{\mathrm{sg}}^2)^{1/2}. \tag{36}$$

Hence, to estimate the accuracy of Eq. (28) as a model, we have to look at the ratio of the remainder $E_2(\mathbf{r})$ to the second term in Eq. (29),

$$\frac{\|E_2\|}{\|s_2\|} \approx \frac{\|Z_{l\mathrm{sg}}\|}{\Delta Z} = \frac{(Z_{\mathrm{sg}}^2)^{1/2}}{\Delta Z}, \tag{37}$$

where

$$\Delta Z = 3 \frac{f''(\overline{Z})}{f'''(\overline{Z})} \tag{38}$$

can be viewed as a characteristic scale in Z space of the particular nonlinearity $f(Z)$. We define

$$\lambda = \frac{(Z_{\mathrm{sg}}^2)^{1/2}}{\Delta Z} \tag{39}$$

and, if λ is sufficiently small, then the error in the ARM approach would be acceptable. Equation (39) can be understood from a different standpoint: given a function $f(Z)$, the value of ΔZ is known from Eq. (38) and, since the value of $(Z_{\mathrm{sg}}^2)^{1/2}$ required for a chosen ratio λ is available from Eq. (39), Eq. (12) can then be used to estimate the required filter size to utilize in the simulation, $\gamma = \Delta_f / 2L_Z$. This approach gives the scaling of the error in the ARM model with the filter size Δ_f. From Eq. (12) we know that $\langle Z_{\mathrm{sg}}^2 \rangle$ varies as $\gamma^{2/3}$. Therefore, since ΔZ does not depend on the filter size, we obtain

$$\lambda \propto \gamma^{1/3}. \tag{40}$$

3. Model coefficient: Spectral variant

The simplest approach is to consider the situation where the subfilter scales are in equilibrium and follow a given spectrum. Working with the Fourier transforms of the scalar field and its filtered values, the coefficients a_i in Eq. (23) are given by integrals in the frequency space involving the scalar spectrum and the filter transfer function, readily computable once a particular spectrum is assumed.[32] The scalar spectrum provides physical information of the subgrid scales, whereas the filter transfer function brings in mathematical information of the filtering operation. The filter transfer function, $\hat{G}(\boldsymbol{\kappa})$ is known, but the scalar spectrum $E_Z(\boldsymbol{\kappa})$ is not. In this case, the scalar spectrum is the input to the ARM model.

The aim of LES is high Reynolds number turbulence, where $E_Z(\kappa)$ in the inertial–convective subrange[42] is described by the Obukhov–Corrsin spectrum, Eq. (11). Several authors[43,44] have studied the behavior of the scalar spectrum and general results for shear flows are that the 5/3-law strictly appears only for Re_λ values beyond 1000, the Obukhov–Corrsin constant tending asymptotically to the value 0.67 (for the three-dimensional spectrum). We consider in this paper only the case $\mathrm{Sc}\lesssim 1$. If $\mathrm{Sc}\gg 1$ a viscous–convective subrange comes up with the Batchelor power law proportional to κ^{-1}; then, the correct new spectrum $E_Z(\kappa)$ is needed in the model formulation.

For high enough Reynolds number and if the filter size is far enough from the large scales of order L_Z and the small scales of order η_Z, it is the inertial–subrange scaling of $E_Z(\kappa)$ that matters. In this situation the flow-dependent large scales are resolved and the shape of the spectrum in the inertial–diffusive or viscous–diffusive subrange, which is unknown with certainty, does not enter because the energy at those scales is already very small. However, in typical turbulent flows, there are regions of the flow with high Reynolds number and other regions with low Reynolds number, and it is desired that the model works smoothly in all parts. Hence, we additionally adopt the shapes of the spectrum for the energy-containing and the diffusive ranges as proposed by Pope[41] for the velocity spectrum

$$f_L(\theta)=\theta^{2+5/3}/(\theta^2+c_L)^{(2+5/3)/2}, \quad \theta=\kappa L_Z,$$
$$f_\eta(\zeta)=\exp(-\beta((\zeta^4+c_\eta^4)^{1/4}-c_\eta)), \quad \zeta=\kappa\eta_Z, \tag{41}$$

so that $E_Z(\kappa)$ can be written as

$$E_Z=Z_{\mathrm{rms}}^2 L_Z C_c \theta^{-5/3} f_L(\theta) f_\eta(\zeta), \tag{42}$$

where $\theta/\zeta=L_Z/\eta_Z=\mathrm{Pe}_t^{3/4}$, the scale η_Z being defined as $\eta_Z=(D^3/\epsilon)^{1/4}$ for the inertial–diffusive subrange. The turbulent Péclet number is defined as $\mathrm{Pe}_t=K^{1/2}L_Z/D$.

The final expression for the model coefficient is[32]

$$c_0=c_0(\gamma,\mathrm{Pe}_t). \tag{43}$$

Thus, if the Reynolds number is not sufficiently large, the model coefficient depends on how the filter length compares with both the large and the small scales of the turbulent motion, a fact that can be expected on physical grounds. Another desirable property is that the scalar spectrum enters just with its unresolved part, i.e., $E_Z(\kappa)(1-\hat{G}^2(\kappa))$, and, since $\hat{G}(\kappa)\approx 1$ for the large scales, the low-wave-number part of the spectrum does not affect the value of c_0; the known nonuniversality of low-wave-number scales does not present a problem. Figure 3 plots the behavior of c_0, given by Eq. (43), for the top-hat filter. We can see the asymptotic behavior of c_0 as Pe_t is increased. This asymptotic value can be computed similarly to the previous estimates of integrals of the spectrum, obtaining

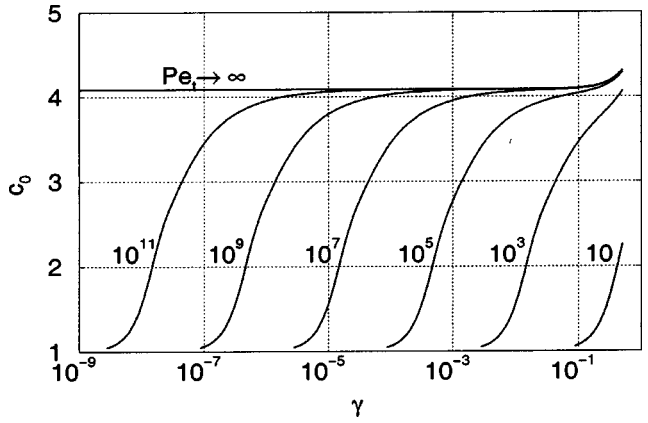

FIG. 3. Dependence of the ARM model coefficient, c_0, on $\gamma=\Delta_f/2L_Z$ for various values of Pe_t. The asymptotic limit at high Pe_t numbers is $c_0=4.1$.

$$\lim_{\mathrm{Pe}_t\to\infty} a_0/(Z_{\mathrm{rms}}^2 C_c \gamma^{2/3}) = \int_0^\infty (1-\hat{G}^2)(\hat{G}^2-1)\xi^{-5/3}\,d\xi$$
$$= -1.0756,$$
$$\lim_{\mathrm{Pe}_t\to\infty} a_1/(Z_{\mathrm{rms}}^2 C_c \gamma^{2/3}) = \int_0^\infty 2(1-\hat{G}^2)\hat{G}^2(1-\hat{G})$$
$$\times\xi^{-5/3}\,d\xi = 0.1383, \tag{44}$$
$$\lim_{\mathrm{Pe}_t\to\infty} a_2/(Z_{\mathrm{rms}}^2 C_c \gamma^{2/3}) = \int_0^\infty (1-\hat{G}^2)(1-\hat{G})^2\hat{G}^2\xi^{-5/3}\,d\xi$$
$$= 0.0305$$

and the value obtained for the model coefficient is $c_0=4.1$, as observed in that figure. Equation (44) shows that the model coefficient for high Péclet numbers depends on the filter and the slope of the spectrum in the inertial subrange. These numbers can be used to calculate the sensitivity of the ARM prediction of the subgrid-scale variance to the model coefficient, given by Eq. (27). The result is $\Gamma=0.27$. It allows us to define an interval for c_0 in order to get a desired accuracy in the prediction of the subfilter variance; for instance, if we want relative errors in the subgrid-scale variance of 10% we need to predict the model coefficient in an interval 0.37 around the value 4.1. The *a posteriori* results in Sec. IV show that this accuracy is attainable.

In an actual LES, the model coefficient c_0 can be precomputed and stored in a two-dimensional table $c_0(\gamma,\mathrm{Pe}_t)$. During the simulation K, Z_{rms} and χ are used to obtain the two parameters γ and Pe_t, a table lookup is performed, and c_0 is obtained. The values of K and Z_{rms} are estimated from the resolved-scale kinetic energy and scalar variance (a cor-

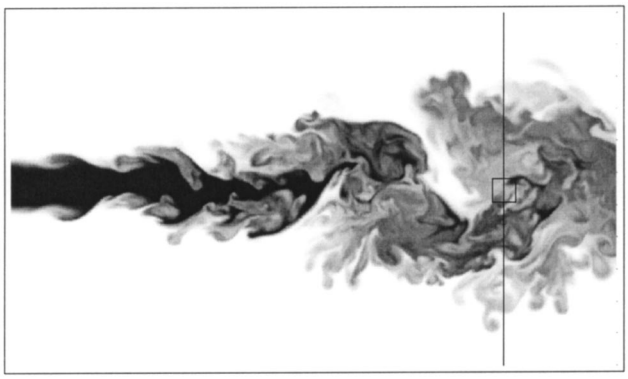

FIG. 4. DNS of a passive scalar. Instantaneous plot of the scalar Z for a plane of constant z. Black corresponds to $Z=1$ and white to $Z=0$. Vertical line indicates the plane $x/h=11.0$ and the square corresponds to the filter volume of $\Delta_f/\Delta_g=16$.

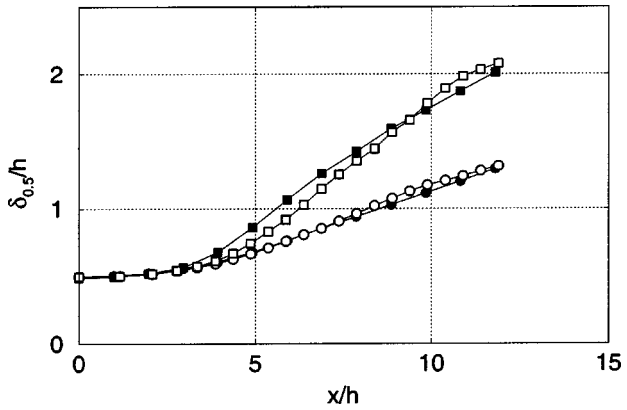

FIG. 5. Evolution of the half-width of the mean profiles. Streamwise velocity: ○, $\langle U\rangle_{\mathrm{DNS}}$; ●, $\langle U\rangle_{\mathrm{LES}}$. Scalar: □, $\langle Z\rangle_{\mathrm{DNS}}$; ■, $\langle Z\rangle_{\mathrm{LES}}$.

rection to account for the subgrid-scale part[41,45] could be used if required) and the value of χ is calculated from the scalar subgrid-scale dissipation, as presented later in Sec. IV.

The difference in this methodology with respect to the original one[32] is only the adoption of the Obukhov–Corrsin spectrum for the scalar field, rather than the Kolmogorov spectrum. The consequences are that the physical parameters entering the model, namely, $\mathrm{Pe}_t=K^{1/2}L_Z/D$ and $\gamma=\Delta_f/2L_Z$ with $L_Z=K^{1/2}Z_{\mathrm{rms}}^2/\chi$, are given by the scalar time scale Z_{rms}^2/χ instead of the velocity time scale K/ϵ, thus reducing the value of Pe_t and increasing γ by about a factor of 2.

III. *A PRIORI* ANALYSIS

A. Description of the DNS

In this section we present results from *a priori* tests using the DNS results of a spatially evolving turbulent plane jet,[46] validated in detail against experimental data. The jet develops in the streamwise coordinate x, with the nozzle, of width h, being located at $x=0$. The crosswise coordinate is y, and the homogeneous spanwise coordinate z. The Reynolds number at the inflow based on the jet width is $\mathrm{Re}_h=3000$, increasing until an approximate value of 4800 near the outflow, which corresponds to a Taylor microscale Reynolds number of 145, defined as $\mathrm{Re}_\lambda=q\lambda/\nu$ with $q^2=2K$ and $\lambda^2=5\nu q^2/\epsilon$. The Schmidt number is 1.0. The size of the physical domain is $15h\times16h\times4h$, being discretized by a grid of $390\times390\times130$ points. In the fully developed region of the jet, the grid spacing compared to the Kolmogorov scale is $\Delta_g/\eta=3.2$. The inflow conditions are as follows. The mean profiles of streamwise velocity and scalar are given by hyperbolic tangent profiles in each shear layer. In addition, a solenoidal fluctuation with broadband spectrum peaking at the most unstable frequency of the spatially evolving shear layer is imposed. Averages are performed in the homogeneous direction z and time. The CPU time for the DNS was about 22000 Cray T3E hours.

Figure 4 shows an instantaneous snapshot of the scalar field. We can see the potential core in the entrance region, the merging of the two shear layers and the transition to the jet zone. The engulfing of exterior irrotational fluid and the richness of scales are clear. Overall quantities are shown in Fig. 5, representing the growth of the jet thickness (based on the half-width values) of the streamwise averaged velocity, $\langle U\rangle$, and the mean scalar $\langle Z\rangle$. The linear growth after an initial region, predicted by the self-similar analysis of the jet in the boundary layer theory, is observed. The LES data in this figure are *a posteriori* results that will be discussed later.

The subgrid-scale model was analyzed at a downstream location $x/h=11.0$, where the flow is fully developed and the small scales near the centerline present a more isotropic behavior. Figure 6 shows the mean, $\langle Z\rangle$, and the root-mean-square, Z_{rms}, at this position. The value of the characteristic parameters entering into the model are $L_Z=K^{1/2}Z_{\mathrm{rms}}^2/\chi=0.82h$ and $\mathrm{Pe}_t=K^{1/2}L_Z/D=475$. As explained in the preceding section, the only input required for the spectral formulation of the ARM model is the actual scalar spectrum. More precisely, only its shape in the subfilter range is required, since the expression for the model coefficient, Eq. (23), is invariant under the multiplication of the spectrum by a constant. Figure 7 shows the scalar spectrum at the centerline of the jet compared to the model spectrum, Eq. (42). The one-dimensional spectrum is obtained from the time series using Taylor's hypothesis. Such a hypothesis is reasonable because, though the downstream coordinate is inhomogeneous, its characteristic scale is large compared with the

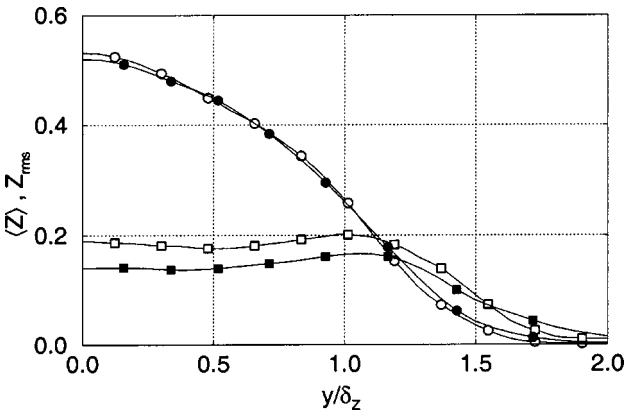

FIG. 6. Profiles of mean, $\langle Z\rangle$, and root-mean-square, Z_{rms}, of the scalar at $x/h=11.0$: ○, $\langle Z\rangle_{\mathrm{DNS}}$; ●, $\langle Z\rangle_{\mathrm{LES}}$; □, $Z_{\mathrm{rms,DNS}}$; ■, $Z_{\mathrm{rms,LES}}$.

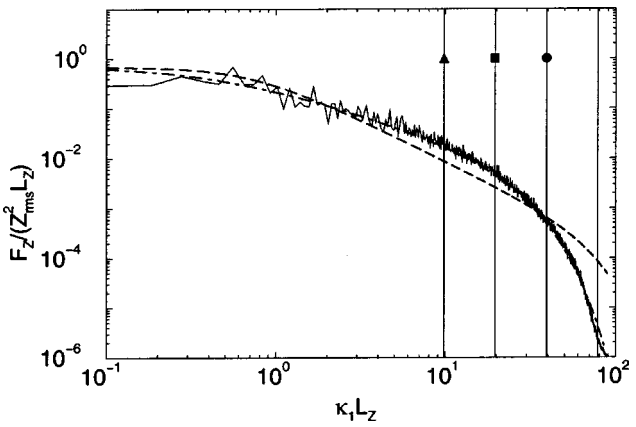

FIG. 7. Scalar 1D spectra, $F_Z(\kappa_1)$: —, DNS spectrum; – – –, general model spectrum; – – –, fit model spectrum. Location of the different filters Δ_f/Δ_g: ●, 4; ■, 8; and ▲, 16. Solid vertical line indicates grid cutoff, $2\Delta_g$.

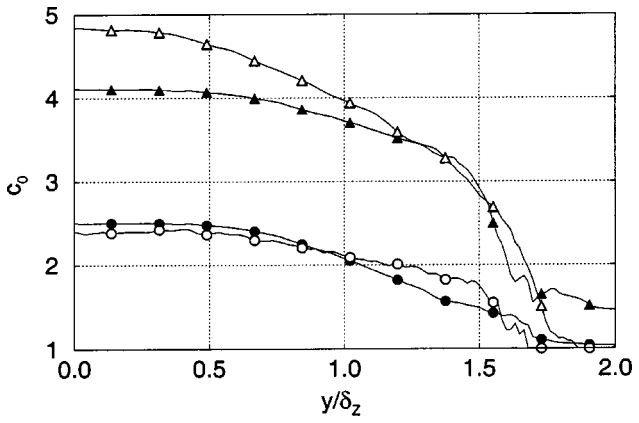

FIG. 8. Predictions of the ARM model coefficient. Hollow symbols correspond to exact values and solid symbols to ARM model predictions (assumed spectrum). Circles and triangles denote filter sizes of 4 and 16, respectively.

crosswise one, which in turn is larger than the subfilter scales we are interested in. It is observed that the model scalar spectrum does not represent accurately the actual one, which is expected given the low Péclet number of the flow and the proximity of the inflow boundary. Interestingly, the model energy spectrum is a better approximation to the DNS value of $E(\kappa)$, the turbulent kinetic energy spectrum, than to the corresponding scalar one, $E_Z(\kappa)$. The filter sizes Δ_f considered are $4\Delta_g$, $8\Delta_g$, and $16\Delta_g$, with Δ_g denoting the grid spacing, and the characteristic length ratios are shown in Table I, along with the typical values of the subgrid-scale fluctuations.

B. Performance of the ARM model

The following results were obtained discretizing the filtering operation by a Simpson rule and using a uniform grid with the same resolution as the DNS, instead of the coarser one used in a LES. The difference is the energy contained in the lobes of the top-hat filter transfer function, which can be estimated to be less than 1% of the subfilter energy, as explained in Appendix C. Besides, the use of the DNS grid reduces the aliasing error due to the numerical calculation of the different nonlinearities; from this point of view, the *a priori* analysis gives an upper bound to the accuracy of a LES, where this resolution power is unavailable. The three-dimensional filtering is done by applying a one-dimensional filtering consecutively in each direction.

TABLE I. Filter sizes. Δ_f is the filter size and Δ_g the grid spacing. h is the nozzle width, δ_Z indicates the half-width of the jet, η_Z denotes the Batchelor scale, and γ is defined by $\Delta_f/2L_Z$. Subfilter variances correspond to the centerline.

Δ_f/Δ_g	Δ_f/h	δ_Z/Δ_f	Δ_f/η_Z	$\gamma\times10^2$	$\langle Z_{sg}^2\rangle$	$\langle Z_{sg}^2\rangle/Z_{rms}^2$
4	0.13	15.0	12.8	2.06	0.007	0.17
8	0.26	7.5	25.6	4.13	0.013	0.32
16	0.53	3.8	51.2	8.26	0.020	0.50

1. Prediction of the model coefficient and subgrid variance

The only input to the spectral formulation of the ARM model is the one-dimensional spectrum $F_Z(\kappa_1)$. Figure 7 shows the actual one as obtained from the DNS. This is related to the three-dimensional scalar spectrum $E_Z(\kappa)$, entering the expressions for the coefficients a_i in Eq. (23), by[42]

$$E_Z(\kappa) = -\kappa \frac{dF_Z(\kappa)}{d\kappa} \tag{45}$$

if isotropy is assumed. However, for this low Péclet number flow, the general expression of $E_Z(\kappa)$ proportional to $\kappa^{-5/3}$ is invalid, and a curve fit to the spectrum given by the DNS is used. This fit yields

$$F_Z \propto \frac{1}{(0.5+\theta)^{1.2}} \exp(-9\zeta^{1.5}), \tag{46}$$

which was used to calculate E_Z with Eq. (45) and obtain the results shown in this section.

The model coefficient for different filter sizes is shown in Fig. 8. Only half of the profile is shown for clarity. It is observed that the agreement between the exact $c_0(y)$ and the value obtained with an assumed spectrum is very good for the small filter size, $\Delta_f/\Delta_g=4$, but there is certain underprediction for the case of $\Delta_f/\Delta_g=16$. The reason is that the assumption of isotropy for the range of subfilter scales is invalid for large filter sizes. This underprediction will be reflected in the results to be presented in the following, and it will be studied in Sec. V, where the different sources of error in the ARM approach are reviewed.

Figure 9 shows the effect of the filter size on the subgrid-scale variance. As the filter size increases, the assumed spectrum and isotropy condition are less accurate and precision diminishes, consistently with the underprediction of the model coefficient shown in Fig. 8. That same graph shows the poorer result given by the scale similarity model, expected from the considerations seen in Sec. II. The test filter used in the scale similarity model was twice the filter size $\Delta_f/\Delta_g=16$, using as coefficient the value[29] of 1.305^2.

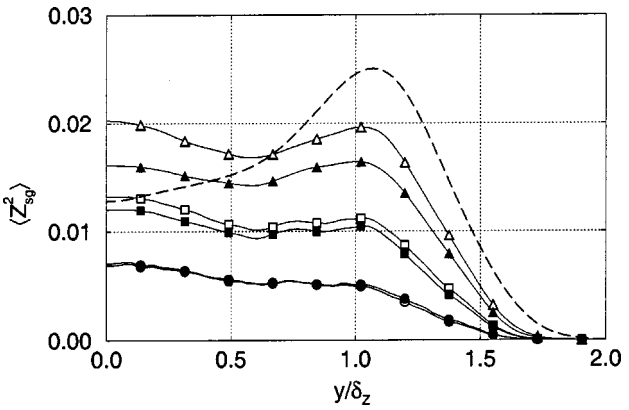

FIG. 9. Prediction of the SGS variance. Hollow symbols correspond to exact values and solid symbols to ARM model predictions. Circles, squares, and triangles denote filter sizes of 4, 8, and 16, respectively. Dashed line indicates the SSM model prediction for $\Delta_f/\Delta_g=16$.

In order to study the instantaneous local behavior, scatter plots of the pointwise prediction of the ARM model and the exact values derived from the DNS were considered. For a fixed crosswise location, the data sequence obtained by the model (M) for different spanwise positions and times was compared with the corresponding exact DNS values (E), calculating the correlation coefficient by

$$C_{EM}=\frac{\langle EM\rangle-\langle E\rangle\langle M\rangle}{\sqrt{(\langle E^2\rangle-\langle E\rangle^2)(\langle M^2\rangle-\langle M\rangle^2)}}. \tag{47}$$

For the subfilter variance, the study was done at the center of the jet, where its value is maximum, and the results are gathered in Table II. ARM provides higher correlation coefficient, 0.89, than the scale similarity model, 0.71. The scale similarity coefficient can adjust the slope of the regression, but not the correlation coefficient. Similar conclusion can be drawn from Fig. 10, which shows the contour plot of the field $Z_{sg}^2(\mathbf{x})$. It can be seen, first, that reconstruction works, and, second, that ARM achieves a significant improvement over SSM by including only one additional filtering operation.

To conclude this part of the discussion, the realizability condition of $0\leqslant Z_M\leqslant 1$, satisfied by the original field Z, was studied. This boundedness of the intermediate field is not strictly required since we are not looking for Z, but is definitely desirable since some of the functions $f(Z)$ only make sense for values of its argument between 0 and 1. When this condition was violated, Z_M was artificially clipped to that interval. At the center of the jet the condition $Z_M<0$ occurred less than 1% of the times, whereas the situation $Z_M>1$ happened less than 2%, both being very low values. The behavior at the edges of the jet was less smooth, and the frequency of Z_M being negative was an order of magnitude higher. The reason is the strong gradient of $Z(\mathbf{x})$ at the viscous superlayer.

TABLE II. Correlation coefficients obtained with the ARM model for polynomial nonlinearities $Y(Z)$. Subfilter and total terms (subfilter+resolved) are shown for different power degrees.

Δ_f/Δ_g	Z_{sg}^2	Z_{sg}^4	Z_{sg}^8	$\overline{Z^2}$	$\overline{Z^4}$	$\overline{Z^8}$
4	0.97	0.97	0.96	1.00	1.00	1.00
8	0.93	0.93	0.93	1.00	1.00	0.99
16	0.89	0.89	0.88	1.00	0.99	0.95

2. ARM performance for polynomial terms

The first type of nonlinearity analyzed is a power function,

$$Y(Z)=Z^n, \quad n=2,3,\ldots. \tag{48}$$

The motivation for these polynomial functions is twofold. First, the algebraic dependence of the reaction rate on the species mass fractions. The reaction rate of a particular elementary reaction step in a reacting flow involving N species is generally described by[2]

$$\omega=k_r\prod_{j=1}^{N} c_j^{\nu_j'}, \tag{49}$$

where c_j denotes the concentration of the species j, related to the species mass fraction Y_j through $c_j=\rho Y_j/W_j$ with W_j being the molecular weight of the species j, and k_r is the *specific reaction-rate constant*. The exponents ν_j' are the stoichiometric coefficients of the reactants in that reaction step. This study considers a nonlinear function Z^n as a first step to see the ability of the ARM model to predict the subgrid-scale part of the reaction rate coming from the dependence on the species mass fractions.

The second motivation arises from the presumed PDF approach, to be discussed later, that requires the input of a certain number of subgrid-scale moments, $\{\overline{Z^n}-\overline{Z}^n, n=2,3,\ldots\}$, in order to define the PDF.

The function $Y(Z)=Z^4$ is now considered. In terms of the reaction rate dependence on the species mass fractions, more typical of reacting systems are the cases Z^2 or Z^3, and the case Z^4 can be thought of as a worst-case scenario. Figure 11 presents the expected value of the subgrid-scale contribution, $Y(Z)_{sg}$, for different filter sizes. Similarly to the variance, deviations of the model prediction with respect to the exact profile increase as the filter size increases, going from 3% to about 20% for the largest filter size of $\Delta_f/\Delta_g=16$. In principle, part of the error is due to the underestimation of the variance, observed in Fig. 9, and some part is intrinsic to the nonlinearity, i.e., due to the assumption underlying Eq. (28). Figure 11 also displays the prediction using the exact model coefficient. By exact model coefficient we mean the profile $c_0(y)$ obtained directly from the DNS data by Eq. (22) without assuming any model spectrum. In this case the agreement is very good, showing that the differences between the ARM prediction and the DNS result is, in these cases, mainly due to inaccuracy in $c_0(y)$.

Correlation coefficients were calculated at the centerline, where the subfilter part of these polynomial nonlinearities achieves its maximum value. The results are shown in Table II. It is seen that the values of C_{EM} for Z_{sg}^4 are similar to those of the variance, of the order of 0.90, indicating again that this type of nonlinearity is well predicted by the reconstruction procedure due to the smoothness of Z^4. We have

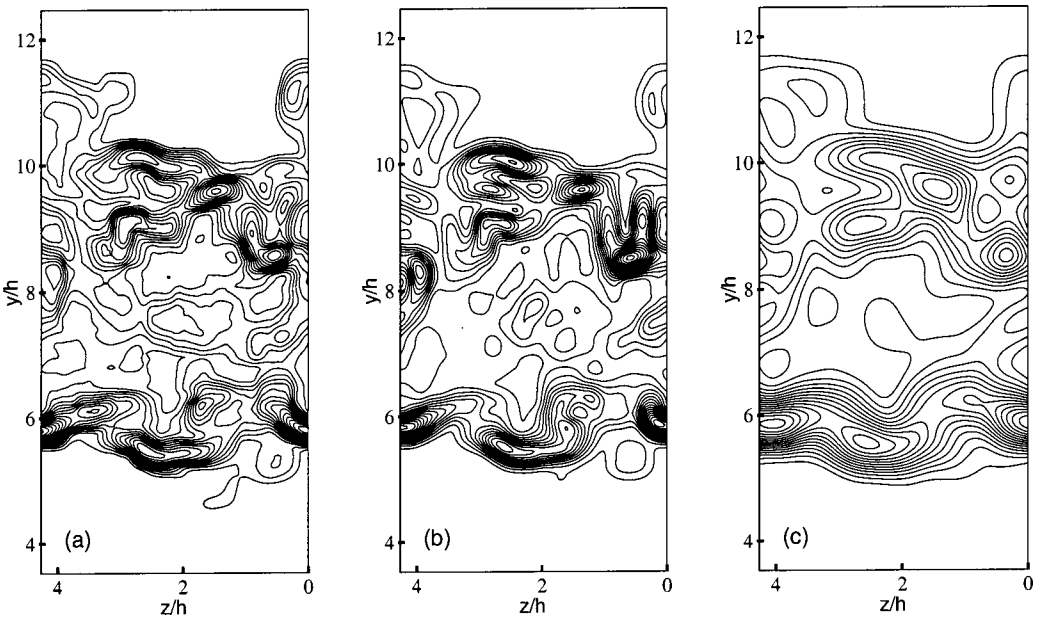

FIG. 10. Contour plots of the field $Z_{sg}^2(\mathbf{x})$ at the plane $x/h=11.0$ (jet is coming perpendicular through the paper). (a) Exact DNS, (b) ARM model, (c) SSM model.

included in that same table the correlation coefficients of the total term $\overline{Z^4}=\overline{Z}^4+Z_{sg}^4$, which is the actual one entering in the governing equations; C_{EM} is increased with respect to the subgrid-scale one since we add an exact term that is larger ($\langle\overline{Z^4}\rangle=0.079$ and $\langle Z_{sg}^4\rangle=0.038$ at the centerline), and the final values are above $C_{EM}=0.99$. The realizability condition, $0\leqslant\overline{Z^4}\leqslant 1$, was always satisfied.

To observe the effect of higher power degrees, the case $Y(Z)=Z^8$ was considered, the resulting correlation coefficients being shown in Table II. In the case of the subgrid-scale field, Z_{sg}^8, the values of C_{EM} are very much like those of Z_{sg}^4, of the order of 0.90. However, the ones of the total term $\overline{Z}^8+Z_{sg}^8$ are reduced compared to the fourth-degree case, though they stay above 0.95. The reason for this decrease of C_{EM} in the total term is that the resolved part is now smaller than the subgrid-scale part, $\langle\overline{Z^8}\rangle=0.0062$ compared to $\langle Z_{sg}^8\rangle=0.032$ at the centerline of the jet, and the exactness of the first one contributes less to the total term than in the case Z^4.

The conclusion from this analysis is that the ARM model is a highly accurate procedure to recover the subgrid-scale part of polynomial terms (at least until degrees of order eight). The reason is that the leading order term in the Taylor's formula Eq. (29) involves the dominant part of the subgrid-scale contribution. Errors in predicting the expected value, $\langle Y(Z)_{sg}\rangle$, in the case of a polynomial nonlinearity are primarily due to inaccuracies in estimating the model coefficient c_0 in the reconstruction procedure. In case of using the spectral variant of ARM, these errors are expected to decrease as the Péclet number increases and the scalar spectrum in the subgrid-scale range tends to a more isotropic form.

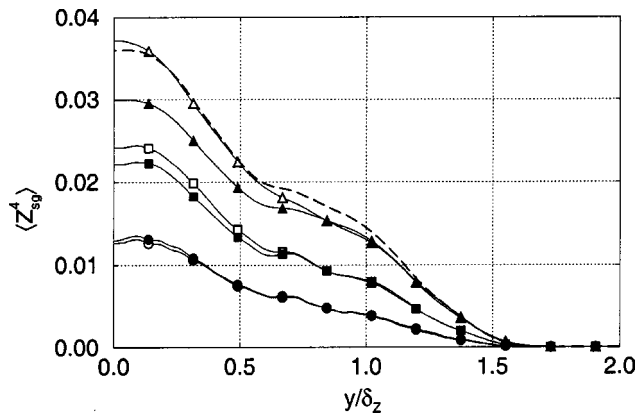

FIG. 11. Prediction of the SGS part of $Y(Z)=Z^4$. Hollow symbols correspond to exact values and solid symbols to ARM model predictions. Circles, squares, and triangles denote filter sizes of 4, 8, and 16, respectively. Dashed line indicates prediction for $\Delta_f/\Delta_g=16$ using the exact $c_0(y)$.

3. ARM performance for infinitely fast chemistry

In the conserved scalar approach to turbulent combustion, the density is the coupling between the chemical part of the problem and the fluid dynamical part,[5] and $\rho(Z)$ is of major interest, Z being the mixture fraction. Under the assumption that pressure and molecular weight of the mixture are approximately constant, the density varies with the temperature as

$$\rho(Z)=1/T(Z). \tag{50}$$

In a further step, the Burke–Schumann approximation[2] leads to a piecewise linear dependence of $T(Z)$ with a peak value of the adiabatic flame temperature T_f at the stoichiometric mixture fraction Z_{st}. The two functions, $T(Z)$ and $\rho(Z)$, are considered. A third interesting nonlinearity comes from the radiation phenomena, enhanced by the high temperatures. A case representative of the optically thin regime was treated

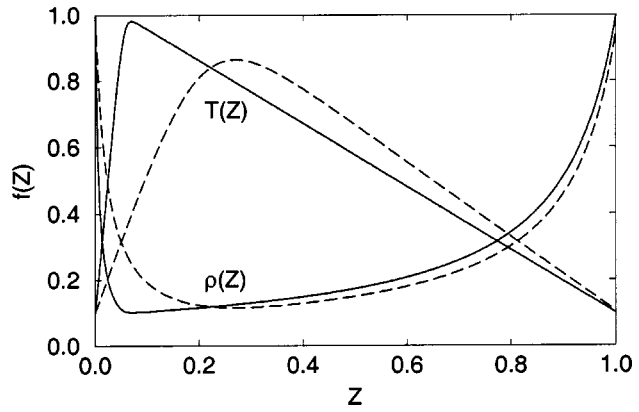

FIG. 12. Profiles of density $\rho(Z)$ and temperature $T(Z)$ considered in the study. Solid line corresponds to $Z_{st}=0.055$ and dashed line to $Z_{st}=0.2$.

by the function $Q(Z)=T(Z)^4$. However, the shape of this curve is very similar to the Arrhenius term $\omega(Z)$ for activation temperatures T_a around $10T_f$, a nonlinearity that will be covered in the following section, and, therefore, results for $Q(Z)$ are not shown explicitly.

In a methane–air mixture, the stoichiometric mixture fraction is 0.055 and a characteristic value of the adiabatic flame temperature[2] can be taken to be 2200 K, approximately an order of magnitude above standard room temperature. Hence, the function $T(Z)$ considered in the study corresponds to $Z_{st}=0.055$ and $T_f=10$, temperatures being normalized by the cold stream value. This curve, along with the density $\rho(Z)=1/T(Z)$, is shown in Fig. 12. In addition, the temperature gradient across the flame is smoothed by means of a hyperbolic tangent profile[47] over a length $\delta=0.01$ in the mixture fraction space. Sometimes the fuel stream is diluted with inert gases, which increases the value of Z_{st}, and thus the case $Z_{st}=0.2$ and $\delta=0.1$ was also analyzed.

Expected values of the density subgrid-scale part, $\rho(Z)_{\mathrm{sg}}$, are plotted in Fig. 13 for the case $Z_{st}=0.055$. As explained in Appendix A, Eq. (A11), the positive curvature of $\rho(Z)$ implies positive subfilter contribution, as observed

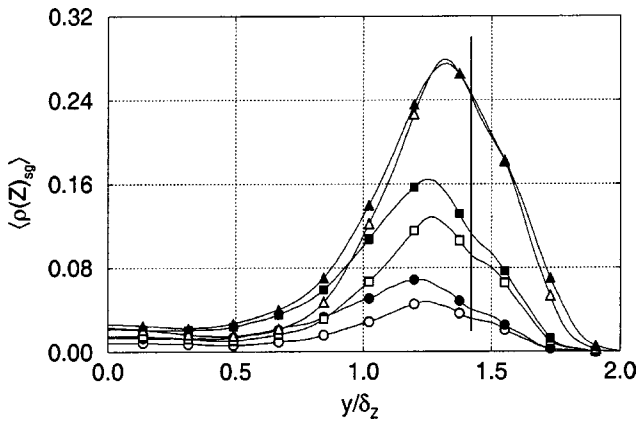

FIG. 13. Prediction of the SGS part of $\rho(Z)$. Hollow symbols correspond to exact values and solid symbols to ARM model predictions. Circles, squares, and triangles denote filter sizes of 4, 8, and 16, respectively. Vertical solid line indicates position of the stoichiometric surface, $\langle Z\rangle=0.055$.

TABLE III. Correlation coefficients obtained with the ARM model for temperature, $T(Z)$, density, $\rho(Z)$. Case (a) corresponds to $Z_{st}=0.055$ and case (b) to $Z_{st}=0.2$.

Δ_f/Δ_g	$T_{\mathrm{sg}}^{(a)}$	$\rho_{\mathrm{sg}}^{(a)}$	$T_{\mathrm{sg}}^{(b)}$	$\rho_{\mathrm{sg}}^{(b)}$
4	0.97	0.94	0.98	0.96
8	0.95	0.92	0.96	0.93
16	0.92	0.90	0.94	0.91

in the results. Accordingly, the sign of the subgrid scale part of $T(Z)$ is negative.

Figure 13 shows that predictions are not as good as the earlier case of polynomial functions, which is to be expected by the strongly nonlinear nature of the function $\rho(Z)$. It is seen in Fig. 12 that there is a characteristic scale $\Delta Z\approx Z_{st}=0.055$ where ρ changes rapidly from 1 to 0.1, whereas the power function $Y(Z)$ varies smoothly with Z. On the other hand, a typical size of the subfilter fluctuation can be estimated from $\langle Z_{\mathrm{sg}}^2\rangle(y)$, plotted in Fig. 9, at the crosswise position where $\langle\rho(Z)_{\mathrm{sg}}\rangle$ is maximum, which yields $\langle Z_{\mathrm{sg}}^2\rangle^{1/2}\approx 0.05$ for the smallest filter size of 4. Since the level of subfilter fluctuation is of the order of ΔZ, the remainder $E_2(\mathbf{r})$ of the expansion in Eq. (29) is relatively large. More detailed analysis of the error will be presented in Sec. V. It was found as well that, in contrast with the polynomial nonlinearity, the error in the ARM model prediction for the density is entirely due to that remainder; the subfilter part was calculated using the exact model coefficient $c_0(y)$ and the result did not differ appreciably from the curves shown in Fig. 13.

The same reasoning applies to the results obtained for the temperature $T(Z)$, which behaves similarly to the density but with opposite sign. The only difference is that the error in the prediction of the averaged profiles of $T(Z)_{\mathrm{sg}}$ is smaller for the smallest filter size, $\Delta_f/\Delta_g=4$, of the order of 10%, and grows with Δ_f, as occurred with the power function, until approximately 20% for $\Delta_f/\Delta_g=16$. For the density, as seen in Fig. 13, the expected value of the subfilter part departs from the exact value at small filter sizes more than it does at large filter sizes, result *a priori* unexpected. Little differences were found between the case of $Z_{st}=0.055$ and $Z_{st}=0.2$.

Correlation coefficients C_{EM} were calculated at the crosswise locations of maximum averaged subfilter parts and are gathered in Table III. They are of the order 0.90 and above, and they decrease with the filter size. It is also shown that the temperature is better predicted than the density by the ARM model. The difference between the case $Z_{st}=0.055$ and $Z_{st}=0.2$ is not very significant, C_{EM} increasing slightly from the first case to the second one due to the smoother profiles of $T(Z)$ and $\rho(Z)$ observed in Fig. 12.

4. ARM performance for the Arrhenius term

The dependence of the specific reaction-rate constant k_r on the temperature T is often given empirically by the Arrhenius law[2]

$$k_r(T)=Ae^{-T_a/T}, \tag{51}$$

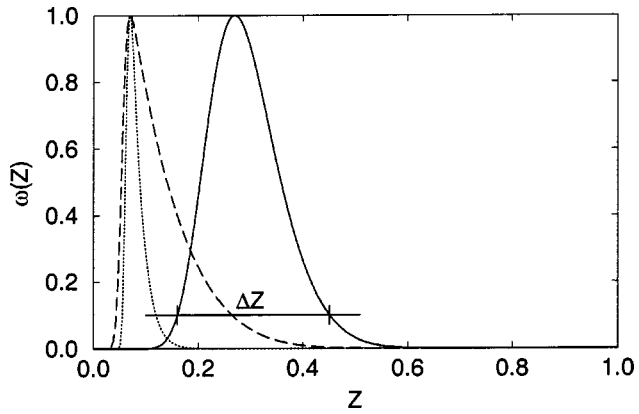

FIG. 14. Arrhenius nonlinearity $\omega(Z)$ considered in the study: —, $Z_{st}=0.2$, $T_a/T_f=10$; – – –, $Z_{st}=0.055$, $T_a/T_f=10$; and ···, $Z_{st}=0.055$, $T_a/T_f=50$. A characteristic scale ΔZ is indicated for the first case.

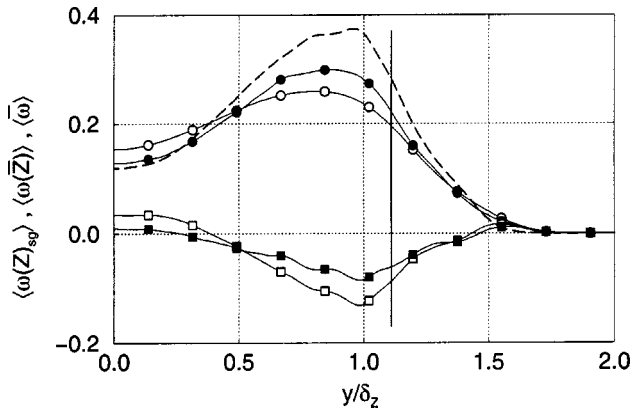

FIG. 16. Different parts of the Arrhenius term with $Z_{st}=0.2$ and $\Delta_f=16\Delta_g$. Hollow symbols correspond to exact values and solid symbols to ARM model predictions: □, ■, SGS part $\langle \underline{\omega}(Z)_{sg}\rangle$; ○, ●, total term $\langle \overline{\omega}\rangle$. Dashed line denotes the resolved part $\langle \omega(Z)\rangle$. Vertical solid line indicates position of the stoichiometric surface.

where T_a is an *activation temperature* and A is the *frequency factor* for the reaction step. The activation temperature is a constant but A can have a weak dependence on T, generally proportional to T^{α}, $\alpha<1$. In this *a priori* analysis, we consider the function

$$\omega(Z)=e^{-T_a/T(Z)} \tag{52}$$

as a starting point to ascertain the ability of the ARM model to predict subgrid-scale contributions to the reaction rate coming from the Arrhenius term. Equation (52) represents a strongly nonlinear function of the mixture fraction Z.

The profiles $T(Z)$ used for this nonlinearity are those of the preceding section, i.e., the cases $Z_{st}=0.055$ and $Z_{st}=0.2$ with $T_f=10$, and an activation temperature of $T_a/T_f=10$ was fixed. An additional (more localized in Z space) situation of $T_a/T_f=50$ at $Z_{st}=0.055$ was also considered. These curves $\omega(Z)$ are shown in Fig. 14.

Expected values of the subfilter part $\omega(Z)_{\mathrm{sg}}$ for the case $Z_{st}=0.2$ are plotted in Fig. 15. For the smallest filter sizes, the agreement between the exact subgrid contribution and the predicted value from the model is good, with errors smaller than or around 10%. But as the filter size is increased

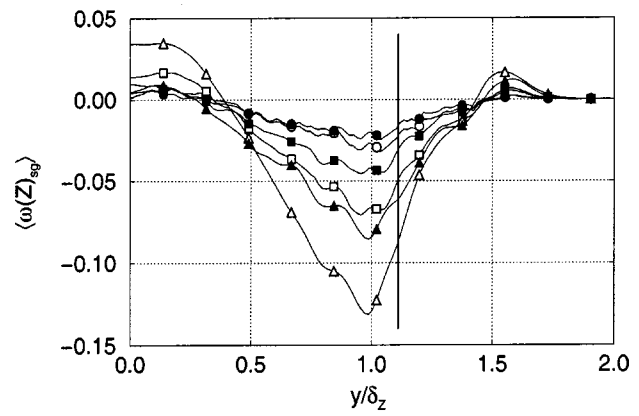

FIG. 15. Prediction of the SGS part of $\omega(Z)$. Hollow symbols correspond to exact values and solid symbols to ARM model predictions. Circles, squares, and triangles denote filter sizes of 4, 8, and 16, respectively. Vertical solid line indicates position of the stoichiometric surface, $\langle Z\rangle=0.2$.

the behavior is poorer, with errors around 30% for $\Delta_f=16\Delta_g$. As in the case of the functions $\rho(Z)$ and $T(Z)$, the error in the ARM model for the case of $\omega(Z)$ is due to the relatively large remainder $E_2(\mathbf{r})$ in Eq. (29) because the predictions using the exact model coefficient $c_0(y)$ were the same. Similar results are obtained for the other two cases of $\omega(Z)$.

Positive and negative subfilter contributions are obtained, accordingly to the alternation of sign in the curvature of $\omega(Z)$, shown in Fig. 14, and the explanation given in Appendix A, Eq. (A11). The physical reason is easy to understand. In the region where the stoichiometric surface is located, $Z\approx Z_{st}$, the additional subgrid-scale fluctuations move the scalar Z toward lower values of $\omega(Z)$ and therefore they tend to decrease $\overline{\omega}$. Similarly, for spatial locations where Z is such that $\omega(Z)\approx 0$, sufficiently large subfilter-scale fluctuations can bring the scalar Z inside the nonzero interval of $\omega(Z)$, and therefore the subgrid-scale part is positive.

Figure 16 shows the expected value of the resolved and subgrid-scale parts of the Arrhenius nonlinearity for the filter size $\Delta_f/\Delta_g=16$. The total term $\overline{\omega}=\omega(\overline{Z})+\omega(Z)_{\mathrm{sg}}$ is the one entering the governing equations, and the prediction given by the ARM model corrects about 60% of the overestimation caused by the resolved part, leading to a final error of about 15%. It is worth noticing that if the mean reaction rate were calculated using only the mean profile $\langle \overline{Z}\rangle$, i.e., using the approximation $\langle \overline{\omega}\rangle\approx\omega(\langle \overline{Z}\rangle)$, it would yield a maximum value of 1 (in these normalized units) at both sides of the jet, where $\langle \overline{Z}\rangle\approx Z_{st}$. However, fluctuations around the mean value are rather large in this flow and such a simplification leads to a substantial overprediction of the peak expected value of the Arrhenius term, since the true maximum shown in Fig. 16 is about 0.3.

With respect to the pointwise behavior of the ARM method in the case of the Arrhenius nonlinearity, scatter plots of model predictions against exact DNS values were obtained for a crosswise location y at which $\langle \omega(Z)_{\mathrm{sg}}\rangle$ was maximum. The correlation coefficients C_{EM}, calculated as

TABLE IV. Correlation coefficients obtained with the ARM model for the Arrhenius term $\omega(Z)$. Case (a) corresponds to $Z_{st}=0.2$ and $T_a/T_f=10$, case (b) to $Z_{st}=0.055$ and $T_a/T_f=10$, and case (c) to $Z_{st}=0.055$ and $T_a/T_f=50$.

Δ_f/Δ_g	$\omega_{sg}^{(a)}$	$\omega_{sg}^{(b)}$	$\omega_{sg}^{(c)}$	$\overline{\omega}^{(a)}$	$\overline{\omega}^{(b)}$	$\overline{\omega}^{(c)}$
4	0.96	0.93	0.85	0.99	0.95	0.71
8	0.92	0.90	0.78	0.93	0.81	0.49
16	0.90	0.87	0.72	0.84	0.56	0.29

previously explained, are gathered in Table IV. Values of C_{EM} for the subgrid-scale part are of the order of 0.90 for the smooth case of $Z_{st}=0.2$, but they decrease for the other two situations, as the characteristic scale ΔZ of the nonlinearity $\omega(Z)$ is reduced, for the same reason explained previously in the case of $\rho(Z)$ or $T(Z)$. With respect to the realizability condition $0\leqslant\overline{\omega}(Z)\leqslant 1$, the first part of the inequality was violated less than 1% of the times and the second only less than 0.03%. However, for the cases of $Z_{st}=0.055$ they increased up to values of 4%, corresponding to the case $T_a/T_f=50$.

Regarding the first case $Z_{st}=0.2$, for filter sizes of 4 and 8, C_{EM} is slightly below the corresponding correlation coefficients for the case of the polynomial nonlinearities, which seems plausible because the Arrhenius term is more nonlinear. However, for the filter size of 16 the ARM prediction for this last nonlinearity correlates better with the exact values than in the case of Z^4 or Z^8. This behavior is, once more, a consequence of the particular shape of $\omega(Z)$. Let us reconsider Fig. 14, which shows that $\omega(Z)$ has a well-defined nonzero region of length ΔZ, and think of a location in the flow domain that has a value of Z that falls into that zone. As one increases the filter size, so does the subgrid-scale fluctuation Z_{sg}^2 and the subgrid-scale contribution to ω (in absolute value). However, when $(Z_{sg}^2)^{1/2}$ becomes of the order of or larger than ΔZ, these fluctuations move the scalar to zones of $\omega\approx 0$ and the subgrid contribution is null regardless of the magnitude of Z_{sg}^2 as long as $(Z_{sg}^2)^{1/2}\gtrsim\Delta Z$. This *saturation phenomenon* is observed as well in the study of the PDF approach, to be discussed later, and is the reason for the insensitivity of the result to the use of the exact model coefficient.

When the resolved part $\omega(\overline{Z})$, known exactly, is added to the subgrid-scale part, the correlation coefficients shown in the last three columns of Table IV vary. If the unresolved contribution is small compared to the resolved one, then C_{EM} increases. However, the improvement in the correlation is not as strong as in the case of the polynomial because of the fact that both parts have opposite signs, and the resulting total term can have values of the order of or smaller than the unresolved part. In this way we see how the correlation coefficient in the case of $\Delta_f/\Delta_g=16$ drops from 0.9 in the case of the subgrid-scale field to 0.84 in the case of the total field of $\omega(Z)$ for $Z_{st}=0.2$.

Cases (b) and (c) in Table IV are more challenging Arrhenius nonlinearities. It can be seen from the corresponding correlation coefficients that only the resolution with $\Delta_f/\Delta_g=4$ (30 points per jet halfwidth) gives good results with the ARM model.

From the preceding discussions of the results for the nonlinearities $\rho(Z)$, $T(Z)$, and $\omega(Z)$, the ratio $\lambda=(Z_{sg}^2)^{1/2}/\Delta Z$ comes up physically as the parameter that defines the range of applicability of the ARM model. This result was already obtained mathematically in Sec. II. The numerator gives the level of fluctuation around the filter value and it is controlled by the filter size. The denominator is the characteristic scale in Z space of the particular nonlinearity and it is dictated by the nature of the nonlinearity.

IV. *A POSTERIORI* ANALYSIS

A. Description of the LES

Large-eddy simulation of a spatially evolving turbulent plane jet has been previously performed[48,49] successfully. In the current work, a LES is conducted to perform an *a posteriori* analysis of the ARM model. A dynamic mixed model is used in the momentum and scalar equations, so that the subgrid-scale stress tensor and the subgrid-scale flux vector are given by

$$\begin{aligned}\tau_{ij}^d&=\rho(\overline{\overline{u_iu_j}}-\bar{\bar{u}}_i\bar{\bar{u}}_j-2\nu_{sg}\overline{S_{ij}^d}),\\ q_i&=\rho(\overline{\overline{u_iZ}}-\bar{\bar{u}}_i\bar{\bar{Z}}-D_{sg}\partial\overline{Z}/\partial x_i),\end{aligned}\tag{53}$$

where $\nu_{sg}=C_d\Delta_f^2|\overline{S}|$, $D_{sg}=C_{Zd}\Delta_f^2|\overline{S}|$, and C_d and C_{Zd} are computed dynamically. S_{ij}^d is the deviatoric part of the strain rate tensor of the filtered velocity field, and $|\overline{S}|$ is defined by $(2\overline{S}_{ij}\overline{S}_{ij})^{1/2}$. This closure of the subgrid terms corresponds to an incompressible case, whereas the simulation was compressible. However, the convective Mach number is 0.16 and the jet had the same temperature as the ambient fluid, incompressibility being therefore a good approximation, sufficient to test the ARM model.

As explained during the introduction of the model, first, having $\overline{Z}$ from the simulation, second, estimating K and $Z_{\rm rms}^2$ from resolved-scale quantities and using the subgrid-scale dissipation for χ to obtain the model coefficient c_0 from a two-dimensional table, we can calculate the subgrid-scale contribution, $\overline{f(Z)}-f(\overline{Z})$, using the ARM model, Eq. (28) and Eq. (20), for any given nonlinear function $f(Z)$. In this flow, averages are taken in the z direction and time, and therefore they are unavailable from the beginning; $c_0=1$ can be assumed initially to build up the required statistics.

The notation follows that of the DNS description. The computational domain is $16h\times 16h\times 4h$, being discretized by a grid of size $64\times 112\times 16$. This yields a ratio of grid spacing between the DNS and LES of $\Delta_g^{\rm LES}/\Delta_g^{\rm DNS}=8$. Since the LES grid can support wavelengths as small as $2\Delta_g^{\rm LES}$ and the dynamic mixed model is applied with the grid filter size, $\Delta_f=2\Delta_g^{\rm LES}$, these LES results should be comparable with results obtained by filtering the DNS with $\Delta_f/\Delta_g^{\rm DNS}=16$, discussed in Sec. III. The test filter used in the implementation of the dynamic procedure is $2\Delta_f$. The numerical algorithm used is a sixth-order compact scheme for the spatial derivatives and a fourth-order Runge–Kutta scheme for the time advancement. The number of grid points in the present

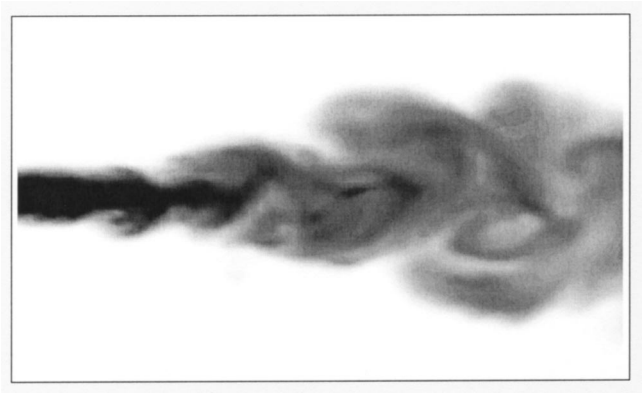

FIG. 17. LES of a passive scalar. Instantaneous plot of the scalar Z for a plane of constant z. Black corresponds to $Z=1$ and white to $Z=0$.

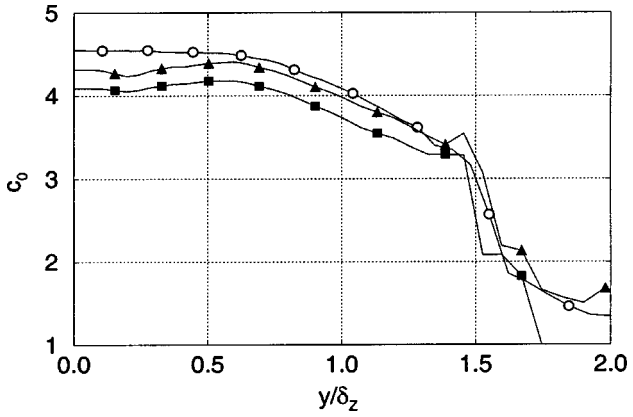

FIG. 18. Model coefficient c_0: ○, *a priori* DNS; ■, *a posteriori* LES; ▲, *a posteriori* LES with correction for K.

LES is 172 times smaller than the DNS, which implies a much lower computational cost. The simulation took about 400 Cray T3E hours. The grid is uniform in the streamwise and spanwise coordinates, x and z, respectively. In the cross-stream coordinate, y, a small stretching of 2.5% is utilized in order to have enough resolution in the shear layers at the inflow. This stretching implies nonuniformity of the filter, and therefore noncommutativity between the derivative and the filter operations in y, but the associated error has been shown to be negligible for these levels of inhomogeneity.[48] The Schmidt number is unity.

In Fig. 17 an instantaneous snapshot of the scalar field from the LES is presented. Comparing with the DNS case in Fig. 4, the truncation in the range of resolved scales is obvious. Nevertheless, the general structure of the jet is preserved, showing large-scale structures and engulfing of exterior irrotational fluid. The growth of the jet is shown in Fig. 5, along with the DNS results. As previously reported,[48,49] the agreement is good. The small departures are due to the difference in the inflow conditions (filtering of the broadband fluctuation field), which is strongly felt in this initial region of the jet. Figure 6 shows the mean profile, $\langle \overline{Z} \rangle$, and root-mean-square profile, $\overline{Z}_{\mathrm{rms}}$. The fluctuation about the mean in the LES is smaller because the subgrid-scale contribution is not taken into account in that plot.

B. Performance of the ARM model

The model coefficient c_0 is shown in Fig. 18, where *a posteriori* results are compared with the value obtained from the DNS data. The difference with the *a priori* analysis is the utilization of resolved values of turbulent kinetic energy, scalar variance and subgrid scalar dissipation. The inputs to the ARM model are a characteristic time, $\overline{Z}^2_{\mathrm{rms}}/\chi$, and a velocity scale, $K^{1/2}$. The first one might be expected to be well represented by $\overline{Z}^2_{\mathrm{rms}}/\chi_{\mathrm{sg}}$, i.e., using the resolved scalar variance and the subgrid-scale dissipation, $\chi_{\mathrm{sg}}=-\langle 2q_i \partial \overline{Z}/\partial x_i \rangle$. The latter has the deficit of the unresolved scales. As a consequence, the model coefficient is slightly below the result obtained from the DNS analysis, as can be seen in Fig. 18. This underprediction can be compensated by the estimate of the total kinetic energy, K, from the resolved part, K_r, using the methodology explained in Pope.[41] In a similar way to the integral analysis of previous sections we end up with

$$\frac{K_r}{K}=1-2.1640\gamma^{2/3}, \tag{54}$$

for the case of a top-hat filter plus a sharp spectral cutoff at $2\pi/\Delta_f$ and valid only for high Reynolds numbers when the filter size is well inside the inertial subrange. The value of the Kolmogorov constant was set to $C_k=1.5$. These conditions do not hold in this particular low Reynolds number flow and we need to use a more specific kinetic energy spectrum, a good approximation being the one given by Eq. (42). For the case of the velocity spectrum, the required parameters are $\mathrm{Re}_t=K^2/\nu\epsilon=1157$ and $L=K^{3/2}/\epsilon=2.0$, as obtained from the DNS data. The ratio is

$$\frac{K_r}{K}=0.6032. \tag{55}$$

This result was checked once the LES was performed, comparing directly with the value of K from the DNS, obtaining a ratio of 0.64 and confirming the estimate above. The compensated model coefficient profile is shown in Fig. 18 and we see that it is very close to the *a priori* result. This *a priori* profile of $c_0(y)$ was computed with the DNS values of Z^2_{rms}, χ and K considering the filter size $\Delta_f(y)$ corresponding to the LES grid. The deviation of the value of c_0 obtained *a posteriori*, remaining after the correction in the turbulent kinetic energy is applied, is due to the approximation $Z^2_{\mathrm{rms}}/\chi \approx \overline{Z}^2_{\mathrm{rms}}/\chi_{\mathrm{sg}}$ and is found to be about 6%. However, the sensitivity of the ARM model to these small variations of c_0 is observed to be very small, as shown in Sec. II, and therefore the ARM approach in the *a posteriori* context maintains the high accuracy observed in the *a priori* one, even if the correction on K is not used.

Figure 19 shows the expected value of the subgrid-scale variance as well as the total variance across the jet at $x/h=11.0$ obtained from the LES. The subgrid-scale variance is well predicted by the ARM model. In order to obtain $\langle \overline{Z}^2 \rangle$ correctly, in addition to predict $\langle Z^2_{\mathrm{sg}} \rangle$ accurately, it is necessary to obtain the variance of the resolved scales, $\overline{Z}^2_{\mathrm{rms}}$, precisely, as shown below. By definition,

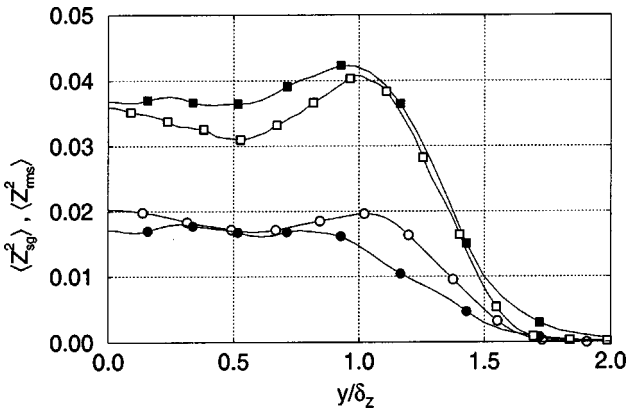

FIG. 19. *A posteriori* and filtered DNS values of scalar fluctuations. SGS part: ○, $\langle Z^2_{sg}\rangle_{DNS}$; ●, $\langle Z^2_{sg}\rangle_{LES}$. Total fluctuation: □, $Z^2_{rms,DNS}$; ■, $\overline{Z}^2_{rms,LES}+\langle Z^2_{sg}\rangle_{LES}$.

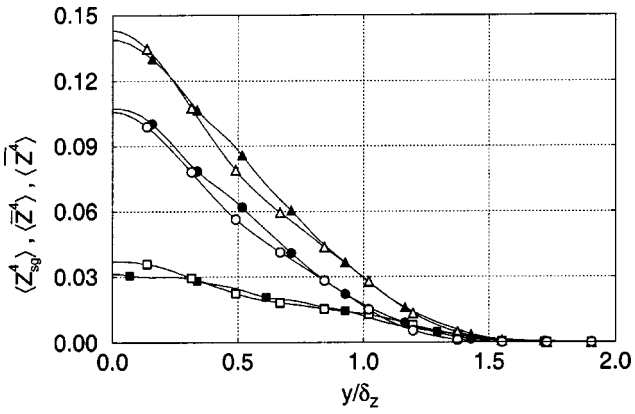

FIG. 20. SGS model performance in predicting $\langle\overline{Z^4}\rangle$. Hollow symbols denote filtered DNS values and solid symbols are LES results: ○, ●, resolved term $\langle\overline{Z^4}\rangle$ (no SGS model); □, ■, SGS term $\langle Z^4_{sg}\rangle$; ARM model; △, ▲, total term, $\langle\overline{Z^4}\rangle=\langle Z^4\rangle+\langle Z^4_{sg}\rangle$.

$$\overline{Z^2}=\overline{Z}^2+Z^2_{sg}. \tag{56}$$

Taking the average of both sides,

$$\langle\overline{Z^2}\rangle=\langle\overline{Z}^2\rangle+\langle Z^2_{sg}\rangle$$
$$\Rightarrow\langle\overline{Z^2}\rangle=\langle\overline{Z}\rangle^2+\overline{Z}^2_{rms}+\langle Z^2_{sg}\rangle$$
$$\Rightarrow\langle\overline{Z^2}\rangle-\langle\overline{Z}\rangle^2=\overline{Z}^2_{rms}+\langle Z^2_{sg}\rangle. \tag{57}$$

The second equality in the above equations follows from the definition of the root-mean-square of the scalar. In the case of filtering in homogeneous directions, the left-hand side of the last equation in Eq. (57) can be replaced by $\langle Z^2\rangle-\langle Z\rangle^2=Z^2_{rms}$. In our case, the effect of inhomogeneity in the x and y directions is weak because Δ_f/δ_Z is small, so that, finally,

$$Z^2_{rms}\approx\overline{Z}^2_{rms}+\langle Z^2_{sg}\rangle. \tag{58}$$

We initially used a dynamic Smagorinsky model. However, as reported by other authors,[48] it tends to overestimate the resolved-scale variables and fluxes. Therefore, a dynamic mixed model was used so as to obtain $\overline{Z}^2_{rms}$ correctly. The results are shown in Fig. 19, where both sides of the Eq. (58) are plotted, showing the good agreement.

The correct prediction of the subgrid-scale variance and the resolved field implies a behavior of the ARM model regarding other nonlinearities very similar to the one observed in the *a priori* analysis. Figure 20 shows the expected value of the resolved (no subgrid-scale model), subgrid-scale and total values corresponding to the function $Y(Z)=Z^4$. As before, the profiles are expected to be symmetric and only half of the extent is shown for clarity. It can be observed that the agreement with the profiles obtained from the filtered DNS is remarkable. The accuracy of the unresolved part is due to the ARM model, whereas the good prediction of the resolved part $\overline{Z^4}$ comes from the dynamic mixed model employed in the closure of the momentum and scalar transport equations.

The behavior of the model for the case of the exponential nonlinearity $\omega(Z)$ is shown in Fig. 21, where the expected value of the resolved, subgrid-scale and total terms is presented. The stoichiometric mixture fraction is $Z_{st}=0.4$. The activation and adiabatic flame temperatures are the same as before, $T_a=100$ and $T_f=10$. The subgrid-scale contribution follows closely the filtered DNS results. The resolved part from the LES does not depart seriously from the DNS result, and therefore the error in the total term $\langle\overline{\omega}\rangle$ is similar to the *a priori* values, less than 10%. Compared to the use of no subgrid model (the line with circles), the results improve significantly using the ARM procedure.

V. ANALYSIS OF THE ERROR IN THE ARM MODEL

The ARM model has two sources of error. The first one comes from the computation of the model coefficient c_0 by Eq. (23), and the second one is due to the use of the intermediate $Z_M(\mathbf{x})$ to compute the subgrid part of the nonlinearity, Eq. (28). These two issues are now explored.

A. Error in the model coefficient

One approximation implicitly assumed for the particular case of turbulent flows with one or more inhomogeneous directions is to consider c_0 constant in the filtering process shown in Eq. (22). In the present case of a turbulent plane

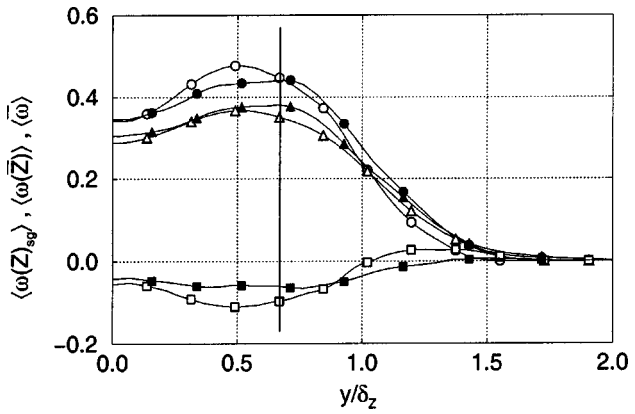

FIG. 21. SGS model performance in predicting the Arrhenius term, $\langle\overline{\omega}\rangle$, with $Z_{st}=0.4$. Hollow symbols denote filtered DNS values and solid symbols are LES results: ○, ●, no SGS model $\langle\omega(\overline{Z})\rangle$; □, ■, SGS term $\langle\omega(Z)_{sg}\rangle$, ARM model; △, ▲, total term $\langle\overline{\omega}\rangle$, ARM model. Vertical solid line indicates position of the stoichiometric surface.

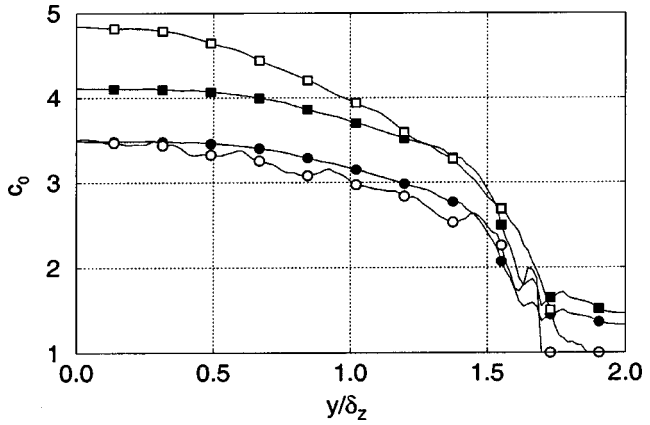

FIG. 22. Predictions of the ARM model coefficient for filter of size $\Delta_f/\Delta_g=16$. 1D filter: ○, exact; ●, assumed spectrum. 3D filter: □, exact; ■, assumed spectrum.

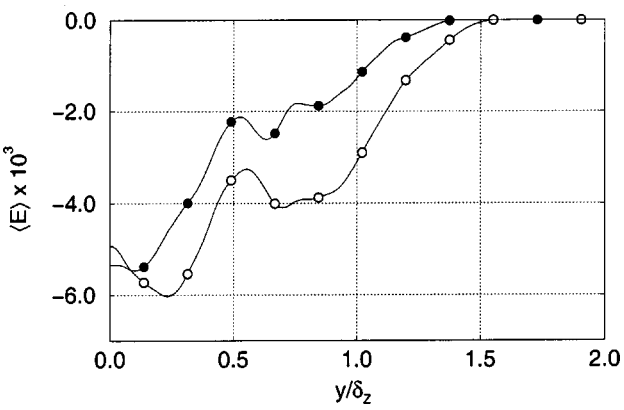

FIG. 23. Error estimate for the polynomial term Z^8 with filter size 16: ○, exact error (exact minus ARM-predicted subgrid part); ●, error prediction from Eq. (35).

jet, the stronger inhomogeneity of the coefficient is in the crosswise y direction (the inhomogeneity in the streamwise x direction is much smaller). However, Fig. 22 shows that the variation of c_0 with y occurs over distances bigger than the filter size Δ_f/δ_Z, shown in Table I, and the error might be reasonably expected to be small.

Second, in Eq. (23), a hypothesis is required to obtain the single unknown term, $\langle (Z^2)_{\mathrm{sg}}\rangle$, to find the coefficient a_0. The case in which the subfilter scales are in equilibrium has been considered, leading to the requirement of the three-dimensional scalar spectrum $E_Z(\kappa)$ in the subgrid range as input to the model. In the present study, a fit to the one-dimensional scalar spectrum $F_Z(\kappa_1)$ obtained from the DNS has been used, Eq. (46), since the Reynolds number is too small to have a good representation of the actual spectrum by the power law $\kappa^{-5/3}$. In order to obtain $E_Z(\kappa)$ from $F_Z(\kappa_1)$ isotropy is assumed, and this is inaccurate. One can study this last hypothesis comparing results from filtering only in the x direction, where the isotropy assumption is not required, with those from filtering in the three directions. This comparison also retains the effect of having an anisotropic filter kernel, $G(\mathbf{x})$.

Figure 22 shows the exact model coefficient, as obtained from the DNS according to Eq. (22), compared to the profile of c_0 yielded by the assumption of a one-dimensional scalar spectrum. We see that the model prediction is exact for the case of a one-dimensional filter, as it should. On the other hand, the agreement in the case of a three-dimensional filter is not as good, indicating that isotropy of the subfilter scalar field is an inaccurate approximation at this Reynolds number and filter size. It is recognized that there are many situations in which either isotropy does not exist (e.g., strong shear or presence of gravity), or the slope of the spectrum is yet unknown (e.g., highly compressible cases), and approaches different to the spectral variant are being derived. Nevertheless, it is always interesting to consider a spectral analysis as a first step because it allows to compute estimates easily and it gives useful insight into the problem.

B. Error in the nonlinearity

The second source of error in the model comes from using the field $Z_M(\mathbf{x})$, given by Eq. (20), as a intermediate to compute the subgrid-scale part for the nonlinearity, $f(Z)_{\mathrm{sg}}(\mathbf{x})$. This step is justified by Eq. (29), the Taylor expansion of $f(Z)(\mathbf{r})$ around the constant function $f(Z(\mathbf{x}))$ inside the cell volume, $\Omega_f(\mathbf{x})$. Therefore, the relative magnitude of the remainder $E_2(\mathbf{r})$ has to be studied for the different nonlinearities. An estimate of the error is obtained from Eq. (35). To retain only the error intrinsic to the nonlinearity, Eq. (28), we work with the exact $c_0(y)$ (obtained directly from the DNS).

The power functions $Y(Z)$, Eq. (48), are considered first. The fourth-degree function has a very small error, and thus the higher order case, Z^8, is considered. Figure 23 shows the exact error, obtained by subtracting the ARM prediction from the exact profile, along with the expected value of $E(\mathbf{x},t)$ as given by Eq. (35). We see that the ARM model provides not only an accurate prediction of the subgrid part of a polynomial term, but a good estimate of the error as well. Besides, $E(\mathbf{x},t)$ gives a pointwise correction of the standard ARM prediction if higher accuracy is desired, at the additional cost of one filtering operation required for calculating $(Z^3)_{\mathrm{sg}}$. If we use Eq. (38) to get a characteristic scale ΔZ for the power functions $Y(Z)$ we obtain the following expression for λ:

$$\lambda_Y=\frac{\|Z_{l\mathrm{sg}}\|}{\Delta Z}=\frac{(n-2)(Z_{\mathrm{sg}}^2)^{1/2}}{3Z}. \tag{59}$$

An estimate of this controlling parameter can be obtained considering $\langle Z\rangle$ and $\langle Z_{\mathrm{sg}}^2\rangle^{1/2}$, this latter bounding from above $\langle (Z_{\mathrm{sg}}^2)^{1/2}\rangle$ according to Eq. (A5). The values are gathered in Table V. It is seen that λ is less than 1, indicating that the first term in the Taylor expansion, Eq. (29), accounts for a major part of the nonlinearity, and therefore the ARM approach provides a good estimate. It is also shown that λ increases with the filter size and with the degree of the polynomial, as expected.

It should be emphasized that these estimates do not give a very precise value of the actual error due to the different simplifications adopted; e.g., $\langle E\rangle/\langle Z_{\mathrm{sg}}^8\rangle\approx 0.18$ at the center-

TABLE V. Estimates of the controlling parameter λ for the different nonlinearities. Case (a) of $\rho(Z)$ corresponds to $Z_{st}=0.055$ and case (b) to $Z_{st}=0.2$, and $\omega(Z)$ corresponds to $Z_{st}=0.2$

Δ_f/Δ_g	Z^4	Z^8	$\rho^{(a)}$	$\rho^{(b)}$	ω
4	0.11	0.32	0.68	0.33	0.63
8	0.14	0.43	1.13	0.50	1.04
16	0.18	0.53	1.54	0.68	1.41

line for a filter size of 16, whereas $\lambda \approx 0.53$. They should be understood only as representatives of the error obtained comparing exact and model subfilter quantities in an *a priori* context, and extrapolate them to work on *a posteriori* problems. What is given by the expression of λ is the scaling of the error in the ARM model with the filter size Δ_f as $\lambda \propto \Delta_f^{1/3}$, expressed by Eq. (40). This scaling means that if we divide the filter size Δ_f by 2, the error in the physical model is reduced by a factor of 1.26. This analytical result agree with the variation of λ with the filter size observed in Table V for the nonlinearity $Y(Z)$.

With respect to the density function $\rho(Z)$, Eq. (50), the expression for λ is

$$\lambda_\rho = \frac{\|Z_{lsg}\|}{\Delta Z} \approx \frac{T'(\overline{Z})(Z_{sg}^2)^{1/2}}{T(Z)} \approx \frac{(Z_{sg}^2)^{1/2}}{Z_{st}}, \tag{60}$$

where terms involving derivatives of $T(Z)$ higher that the first one have been neglected. T'/T can be estimated by $1/Z_{st}$, with $T \approx T_f$. Using the values of $\langle Z_{sg}^2 \rangle^{1/2}$ shown in Fig. 9 at the crosswise location y/δ_Z corresponding to $\langle Z \rangle = Z_{st}$, the values of λ shown in Table V are obtained. It is seen that they are larger than the polynomial ones. The case of $Z_{st}=0.055$ for large filter sizes gives $\lambda \gtrsim 1$, indicating that the ARM model is close to the limit of applicability. As it was said for the case of the polynomial, the value of $\lambda=1$ is not a clear cut between acceptable and unacceptable behavior and these numbers are better understood simply by associating them to the results presented in Sec. III. The second comment to be made is about the effect of Z_{st}, which is clear in the expression for λ: as the stoichiometry decreases, the slope dT/dZ increases on the lean side and a smaller level of subfilter fluctuation, i.e., higher resolution, is required for the ARM model to be successful. This is observed by comparing the values of the parameter λ between the case $Z_{st}=0.055$ and the case $Z_{st}=0.2$.

Let us consider now the case of the Arrhenius nonlinearity $\omega(Z)$, Eq. (52), for $Z_{st}=0.2$. The parameter λ defined by Eq. (39) is

$$\lambda_\omega = \frac{\|Z_{lsg}\|}{\Delta Z} \approx \frac{T_a T'(\overline{Z})(Z_{sg}^2)^{1/2}}{3T(\overline{Z})^2} \approx \frac{(T_a/T_f)(Z_{sg}^2)^{1/2}}{3Z_{st}}, \tag{61}$$

an expression valid for high activation energy, $T/T_a \ll 1$. The estimate of λ is shown in Table V. It was calculated similarly to the case of $\rho(Z)$, i.e., using $T'/T \approx 1/Z_{st}$ and $T \approx T_f$, because the stronger subfilter fluctuations (except for the sharp gradients at the viscous superlayer) appear around the reaction zone (every term in the Taylor's formula has a factor ω). It is seen again that λ is higher in this nonlinearity than in the case of the power function, due to the stronger nonlinear character and implying a larger error in the prediction of the subfilter part of $\omega(Z)$. Apart from the effect of Z_{st}, explained already in the density function, the second important parameter that appears in the expression of λ is the ratio T_a/T_f. It shows that the relative importance of the remainder $E_2(\mathbf{r})$ increases when the activation energy increases, which is expected because $\omega(Z)$ becomes more local. The example is given by the correlation coefficients obtained for the case $T_a/T_f=50$, shown in the *a priori* analysis in Table IV.

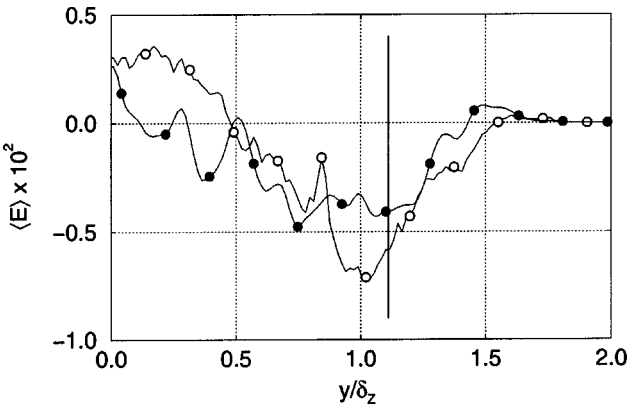

FIG. 24. Error estimate for the Arrhenius term with $Z_{st}=0.2$ and filter size of 4: ○, exact error (exact minus ARM-predicted subgrid part); ●, error prediction from Eq. (35). Vertical solid line indicates position of the stoichiometric surface.

Smaller subfilter fluctuation of the scalar implies better performance of the ARM model, as described by λ, and this is shown in Fig. 24, which represents the Reynolds average of the error estimate $E(\mathbf{x},t)$ given by Eq. (35) along with the actual error in the prediction of $\langle \omega(Z)_{sg} \rangle$, for the case $\Delta_f/\Delta_g=4$. The results in all the figures are nondimensionalized with the instantaneous peak value. Comparing with the total term $\langle \overline{\omega} \rangle$, shown in Fig. 16, the error in the case of the filter size of 16 is about 20%. As we reduce the filter size the accuracy increases, and thus for the case of filter size 4 the error is about 2% of the total term.

It is interesting to consider the case $\omega(T)$, a situation that appears when a conserved scalar approach is not taken. Then, the ratio $(T_{sg}^2)^{1/2}/\overline{T}$ is the one entering in the definition of λ. Figure 25 shows an estimate of this ratio for the case $Z_{st}=0.2$, and it is observed that the subfilter fluctuation of the temperature increases as we approach the edges of the jet. This behavior with the coordinate y is similar in the case of higher stoichiometric mixture fractions, like $Z_{st}=0.5$, which corresponds to the reaction zone being closer to the centerline. Physically, the intermittency of the edge of the jet implies higher probability of having blobs of cold fluid than in the center of the jet, and those are able to produce higher gradients and therefore higher subfilter fluctuations in $T(\mathbf{x})$, even if the flame is not located there. Hence, when the reaction is taking place in the center of the jet the ARM model is expected to perform better than in the case of the stoichiometric surface being on the edge.

Finally, it is worth noticing that in the Reynolds-

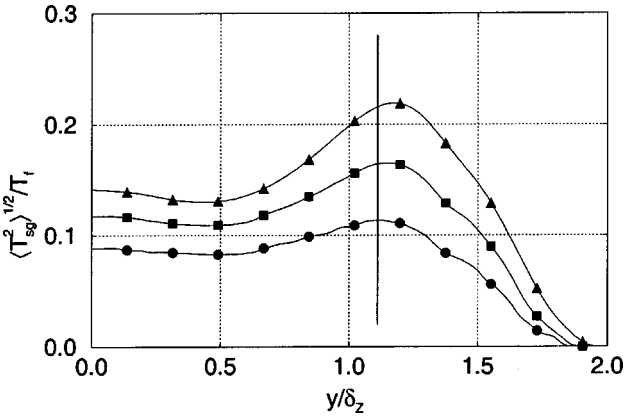

FIG. 25. Subgrid-scale temperature for $Z_{st}=0.2$. Symbols denote different filter sizes Δ_f/Δ_g: ●, 4; ■, 8; and ▲, 16. Vertical solid line indicates position of the stoichiometric surface.

averaged Navier–Stokes (RANS) context, an expression for the mean Arrhenius term can be obtained carrying out a similar expansion of the exponential function,[1] ending up with the requirement $T'T_a/\langle T\rangle^2 \ll 1$, a condition that is not usually fulfilled. The difference between RANS and LES is that, in RANS, the fluctuation T' of the temperature about the mean is fixed by the physical problem, whereas in LES the subgrid-scale fluctuation can be reduced by decreasing the filter size until λ is small enough.

VI. PRESUMED FDF MODEL

A popular subgrid model for turbulent combustion is the so-called *presumed FDF model*. In this approach, the filtering operation is written in terms of a probability density function. Starting from the fine grained PDF,[6,7] $p'(\zeta;\mathbf{x},t)$, one can obtain the filtered fine grained PDF[7] by

$$\overline{p'}(\zeta;\mathbf{x},t)=\int_\Omega \delta(Z(\mathbf{r},t)-\zeta)G(\mathbf{x},\mathbf{r})d\mathbf{r} \tag{62}$$

to write the filtered value of a general nonlinear function $f(Z)$ with $0\leqslant Z\leqslant 1$ as

$$\overline{f(Z)}(\mathbf{x},t)=\int_0^1 f(\zeta)\overline{p'}(\zeta;\mathbf{x},t)d\zeta. \tag{63}$$

The filtered fine grained PDF is a random function because it is defined by a deterministic mapping of the random function Z; for a fixed $(\mathbf{x},t)$ point, the whole curve $\overline{p'}(\zeta)$ will be different in different realizations as a consequence of the random variation of $Z(\mathbf{r})$ from one realization to another. The expected value of a filtered quantity is then given by

$$\langle\overline{f(Z)}\rangle(\mathbf{x},t)=\int_0^1 f(\zeta)\langle\overline{p'}\rangle(\zeta;\mathbf{x},t)d\zeta. \tag{64}$$

The filtered fine grained PDF has been given different names by different authors: the filtered density function,[50] the large-eddy PDF[21] and the subgrid-scale PDF.[23,24] As originally presented,[7] $\overline{p'}(\zeta;\mathbf{x},t)d\zeta$ represents the fraction of the fluid around $\mathbf{x}$ (weighted by G) whose Z concentration is in the range $\zeta\leqslant Z<\zeta+d\zeta$. From now on, we will refer to the filtered fine grained PDF as the filtered density function (FDF) and it will be denoted by $P_Z(\zeta;\mathbf{x},t)$ for notational convenience.

A. Beta-PDF model

In the *presumed FDF* approach the FDF is assumed to follow a prescribed distribution, the beta distribution being the usual choice.[23,24] This is given by

$$P_Z(\zeta;\mathbf{x},t)\approx P_Z(\zeta;\overline{Z},Z''^2_{sg})\approx\frac{\zeta^{a-1}(1-\zeta)^{b-1}}{\int_0^1\zeta^{a-1}(1-\zeta)^{b-1}d\zeta}, \tag{65}$$

where the denominator is the beta function, $B(a,b)=\Gamma(a)\Gamma(b)/\Gamma(a+b)$, and the exponents are given by

$$a=\overline{Z}(\overline{Z}(1-\overline{Z})/Z''^2_{sg}-1),\quad b=a(1/\overline{Z}-1). \tag{66}$$

It is well defined in the sense that the exponents a and b are non-negative at any point of space and instant of time as long as the filter kernel is positive. This is shown as follows. The positiveness of the filter maintains the order relation, and thus $0\leqslant\overline{Z}\leqslant 1$ because $0\leqslant Z\leqslant 1$. Hence, b is positive if a is positive, and this latter is true because of the inequality Eq. (A6). The limiting case $a=b=0$, which corresponds to $Z''^2_{sg}=\overline{Z}(1-\overline{Z})$, has to be handled with more care, since the numerator of Eq. (65) becomes nonintegrable and the denominator of that same equation becomes infinity. A closed expression for $\overline{f(Z)}$ can be obtained by decomposing the function $f(\zeta)$ in a linear part between $\zeta=0$ and $\zeta=1$, $f_0+(f_1-f_0)\zeta$, and a remainder, $R(\zeta)$, so that Eq. (63) yields

$$\overline{f(Z)}=f_0+(f_1-f_0)\overline{Z}+\frac{\int_0^1\zeta^{a-1}(1-\zeta)^{b-1}R(\zeta)d\zeta}{B(a,b)}. \tag{67}$$

This remainder $R(\zeta)$ is zero at 0 and 1, which eliminates the possible singularity of the integrand [assuming $f(\zeta)$ is smooth] in the last term the equation above. Hence, the numerator of this last term is bounded for zero values of a and b, obtaining finally

$$\lim_{a,b\to 0}\overline{f(Z)}=f_0+(f_1-f_0)\overline{Z}. \tag{68}$$

All this information allows the construction of the mapping $\overline{f(Z)}(\overline{Z},Z''^2_{sg})$ for each nonlinearity $f(Z)$, where $0\leqslant\overline{Z}\leqslant 1$ and $0\leqslant Z''^2_{sg}\leqslant\overline{Z}(1-\overline{Z})$. This two-dimensional table is what is required to perform a LES using the FDF approach, and can be computed beforehand and then, given the pair $(\overline{Z},Z''^2_{sg})$ at each point of space and instant of time, interpolation can be used to obtain $\overline{f(Z)}$. This approach was used in the *a priori* results presented below, an approach that was found to provide a better control of the singularities that might appear in the integrand, Eq. (65), and to reduce significantly the time of computation.

1. A priori analysis of the beta-PDF model

The beta-PDF approach involves two assumptions, as it is shown by Eq. (65). The first one is that P_Z depends only on the first two moments, $\overline{Z}$ and Z''^2_{sg}, i.e., different points with the same filtered and variance values have the same P_Z.

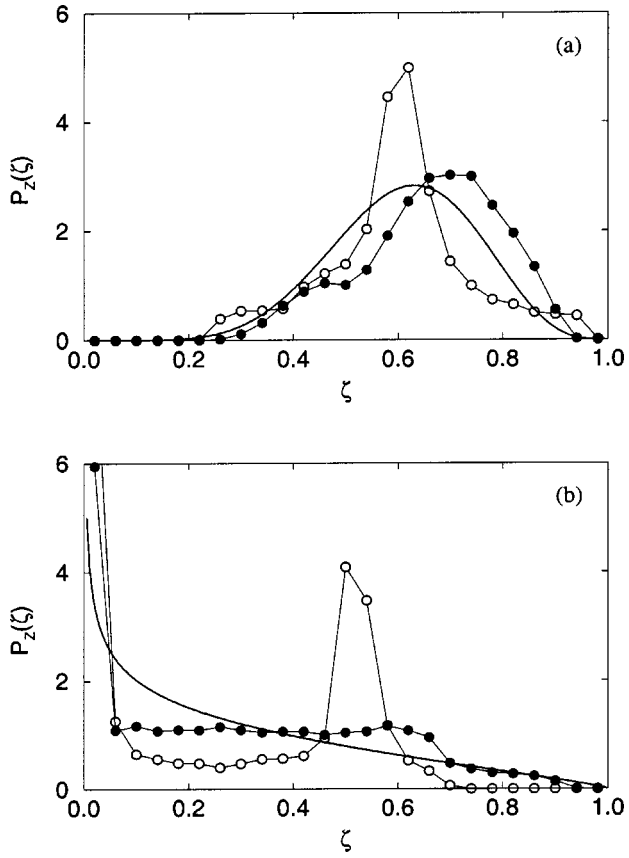

FIG. 26. FDF at (a) the centerline and (b) the jet half-width. Hollow symbols denote FDFs of $Z(\mathbf{r})$ and solid symbols indicate FDFs of $Z_M(\mathbf{r})$ at the same point. The solid line corresponds to the beta-PDF approximation with the exact subfilter variance. Filter size is 16.

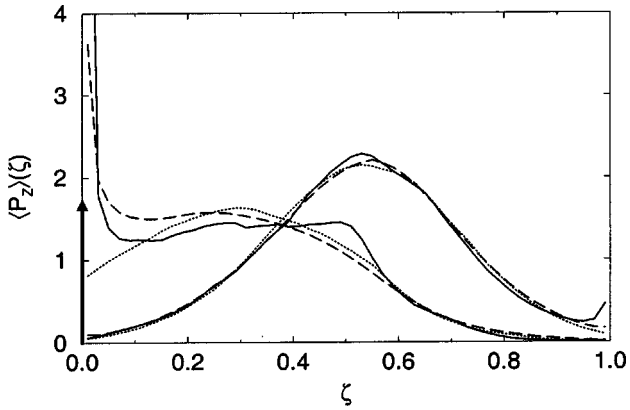

FIG. 27. Averaged FDF at the centerline (right set) and at the half-width of the jet (left set): —, exact; ---, beta PDF; and ···, composite PDF. Filter size is 16.

This is not generally true, and several cases were found where at two different times the scalar field happens to have similar filtered and variance values with the FDF being qualitatively different, showing certain asymmetries or different flatness. The second is that, given that two parameters are sufficient to represent the FDF, P_Z has the particular shape of a beta PDF. Some realizations are described reasonably well by a beta distribution, as shown in Fig. 26(a). However, the beta PDF cannot represent the distribution either near the limits 0 and 1 of the scalar or in case of bimodal distributions; this latter situation is observed in Fig. 26(b).

By definition of the FDF, the ARM approach can be written as

$$\overline{f(Z_M)} - f(\overline{Z_M}) = \int_0^1 [P_{Z_M}(\zeta) - \delta(\zeta - \overline{Z_M})] f(\zeta) d\zeta, \quad (69)$$

where the dependence on $(\mathbf{x},t)$ has been dropped for clarity. Hence, the ARM approach has an associated FDF, $P_{Z_M}(\zeta)$, which is also of interest. Figures 26(a) and 26(b) show the FDF computed at a certain instant of time in the center of the jet and at the crosswise position $y=\delta_Z$. They show the FDF associated with the field $Z(\mathbf{r})$, the original scalar field from the DNS, and the FDF obtained from the intermediate field $Z_M(\mathbf{r})$, obtained using the ARM model with the exact model coefficient $c_0(y)$. Along with those two lines the beta PDF is also plotted. It is striking to see that the FDF of Z_M is similar to the beta distribution with the exact subgrid-scale variance. It should be noted that the ARM procedure has the Reynolds-average subfilter variance as input, rather than the detailed pointwise subgrid-scale variance of the beta-PDF model.

Nevertheless, though the exact FDF is described incorrectly, the results obtained with the presumed FDF model have been found to be fairly good within the *a priori* context.[24,29,30] The reason[24] is that, although the model does not follow the exact FDF, the local deviations balance each other in the integral of Eq. (63) if $f(Z)$ is not very localized (the FDF integrates to one, hence, overestimation in some intervals implies underestimation in others). Furthermore, the estimate of the expected value of the FDF, $\langle P_Z \rangle(\zeta)$, is even better due to the averaging process, as it is shown in Fig. 27, and therefore the prediction of $\langle \overline{f(Z)} \rangle$ is more accurate than the pointwise behavior (the composite-PDF will be define later and the corresponding results in Fig. 27 will be then discussed).

We now discuss our evaluation of the beta-PDF closure with the variance given by the scale similarity model as described in Sec. III, for the nonlinearities $Y(Z)=Z^4$, $\rho(Z)$ for $Z_{st}=0.055$ and $\omega(Z)$ for $Z_{st}=0.2$. Though the FDF model gives the required term $\overline{f(Z)}$ directly, we subtracted the resolved part $f(\overline{Z})$ in order to directly measure the influence of subgrid variations of the scalar. Figures 28 and 29 show the mean profiles for the first two cases and the pointwise behavior is again analyzed with the aid of the correlation coefficients, calculated as in the preceding section and collected in Table VI.

The performance of the FDF model in the case of the polynomial function is very poor, in the average as well as in the pointwise behavior, with a correlation coefficient of 0.41 for the filter size $\Delta_f/\Delta_g=16$. This is less than half the correlation coefficient obtained with the ARM model. Since the nonlinearity $Y(Z)$ is global (characteristic scale $\Delta Z \approx 1$) the source of this error must be the local subgrid-scale variance entering the beta PDF, which was shown before to be poorly estimated by the scale similarity model. If the exact value of the local subgrid-scale variance is employed, the prediction is very good, as shown in Fig. 28.

On the other hand, in the case of the density $\rho(Z)$, the

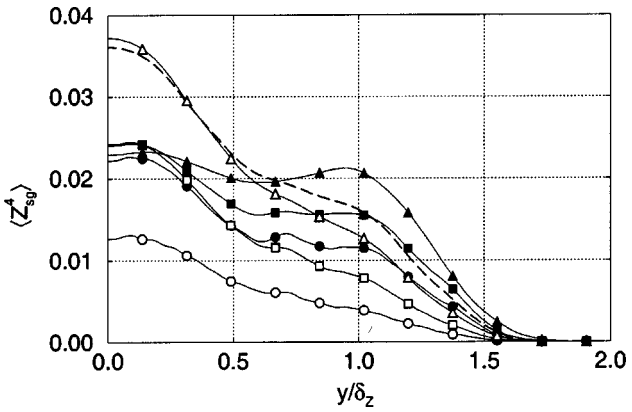

FIG. 28. Predictions of the SGS part of $Y(Z)=Z^4$ by the beta-PDF model. Hollow symbols correspond to exact values and solid symbols to FDF model predictions. Circles, squares, and triangles denote filter sizes of 4, 8, and 16, respectively. Dashed line corresponds to FDF with exact variance for $\Delta_f/\Delta_g=16$.

behavior is different. The expected values of the subfilter part are plotted in Fig. 29 and can be compared to the ARM model results of Fig. 13. For small filter sizes the FDF model overestimates considerably the subgrid-scale part, and the prediction improves as the filter size is increased. The correlation coefficients of Table VI present the same trend. In this case, ARM model yields better results. However, when the exact variance is used, the estimates are very close to the exact values for small filter sizes and, though not shown in that figure for the sake of clarity, they deteriorate as Δ_f becomes larger, as could be expected beforehand. Hence, the error in the FDF model comes from the use of the SSM model to provide the subfilter variance, error that compensates the underprediction of the assumed FDF with the exact variance to give seemingly a good estimate of $\langle \rho(Z)_{\mathrm{sg}} \rangle$ for $\Delta_f/\Delta_g=16$; C_{EM} is, however, relatively low compared to the ARM result shown in Table III.

The nonlinearity $\omega(Z)$ with $Z_{st}=0.2$ presents the same behavior with Δ_f in the average profiles due to the use of the

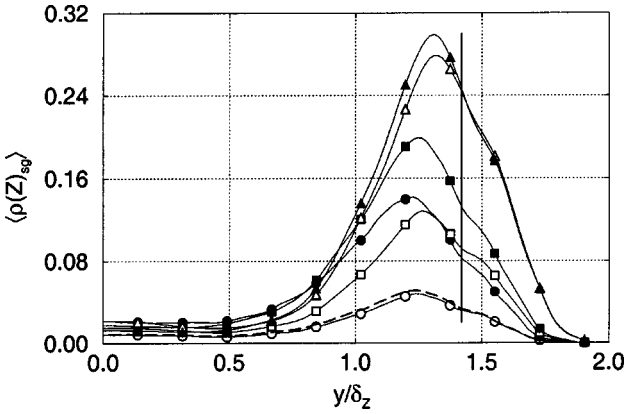

FIG. 29. Prediction of the SGS part of $\rho(Z)$ by the beta-PDF model. Hollow symbols correspond to exact values and solid symbols to FDF model predictions. Circles, squares, and triangles denote filter sizes of 4, 8, and 16, respectively. Dashed line corresponds to FDF with exact variance for $\Delta_f/\Delta_g=4$. Vertical solid line indicates position of the stoichiometric surface, $\langle Z \rangle=0.055$.

TABLE VI. Correlation coefficients with the FDF model for different nonlinearities. The variance was obtained with the SSM model in the case (a) and with the ARM model in the case (b).

Δ_f/Δ_g	$Y^{(a)}_{sg}$	$\rho^{(a)}_{sg}$	$\omega^{(a)}_{sg}$	$Y^{(b)}_{sg}$	$\rho^{(b)}_{sg}$	$\omega^{(b)}_{sg}$
4	0.80	0.84	0.89	0.96	0.93	0.96
8	0.77	0.86	0.91	0.93	0.91	0.95
16	0.41	0.86	0.94	0.88	0.87	0.95

SSM model, though more smoothly indicating a smaller sensitivity to the subgrid-scale variance. It was found as well that the predictions for the large filter size of 16 were better than the ARM model estimates, in the mean profiles as well as in the pointwise behavior, as can be seen by comparing Table IV and Table VI.

Several questions arise from these results. First, how does the sensitivity of the FDF approach to the subgrid-scale variance depend on the nonlinearity $f(Z)$. Second, what is the importance of the particular shape of the assumed FDF, provided that it is a two-moment-based FDF satisfying certain physical requirements. Third, how does a two-moment-based FDF behave as the nonlinearity $f(Z)$ becomes more and more local, i.e., in the limit $\Delta Z \to 0$. These issues are now considered.

2. Sensitivity of the FDF approach to the subgrid-scale variance

As previously exposed, the assumption of a beta-PDF with a given mean, $\tilde{Z}$, and a given variance, Z^2_{sg}, leads to a unique value $f(Z)_{\mathrm{sg}}$ of the subgrid-scale contribution for any given function $f(Z)$, which we refer to as the mapping $f(Z)_{\mathrm{sg}}(\tilde{Z},Z^2_{\mathrm{sg}})$. Figures 30(a) and 30(b) show isocontours of this mapping for the two functions $Y(Z)=Z^4$ and $\omega(Z)$ with $Z_{st}=0.2$. The region defined by the parabola corresponds to Eq. (A6) and it represents all the possible values of the pair $(\tilde{Z},Z^2_{\mathrm{sg}})$ for any point in space at any instant of time. For $Z^2_{\mathrm{sg}}=0$ we have zero unresolved contribution, which is the contour line coinciding with the abscissa axis. For $Y(Z)$ the subgrid-scale part is always positive but, in the case of $\omega(Z)$, the zone around the stoichiometry surface is associated with negative $f(Z)_{\mathrm{sg}}$ while zones sufficiently far away from Z_{st} [out of the region defined by the dashed line in Fig. 30(b)] are associated with positive $f(Z)_{\mathrm{sg}}$, for the reasons explained in Appendix A.

It can be seen that for $Y(Z)$ the contours are approximately parallel to the $\tilde{Z}$ axis, and therefore any error in the prediction of the variance Z^2_{sg} causes appreciable error in estimating the subgrid-scale value.

On the other hand, for the Arrhenius case, the contours around the stoichiometric surface $\tilde{Z}=Z_{st}=0.2$ are more or less parallel to the ordinate axis once Z^2_{sg} is above certain threshold, about 0.01 in this particular case. This means that large variations of the subgrid-scale variance do not change the subfilter contribution $\omega(Z)_{\mathrm{sg}}$ very much. The physical reason was already seen in Sec. III. The filter sizes considered in this *a priori* study correspond to average values of subgrid-scale fluctuation not much larger than this threshold

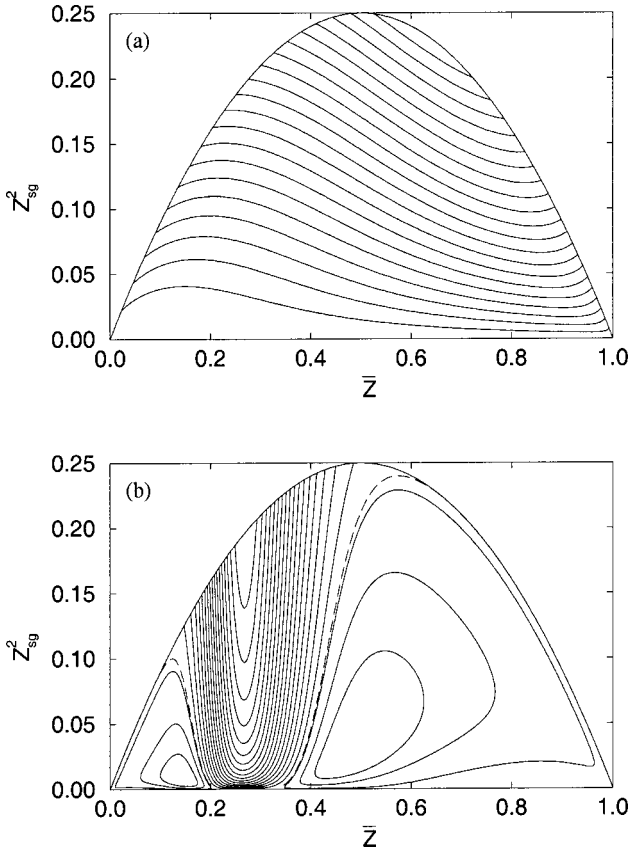

FIG. 30. Beta-PDF mappings $f(Z)_{sg}(\bar{Z},Z^2_{sg})$ for the functions: (a) $Y(Z)=Z^4$, (b) $\omega(Z)$ for $Z_{st}=0.2$. The isocontours represent constant SGS value, $f(Z)_{sg}$. The dashed line indicates zero SGS part.

(Table I shows $\langle Z^2_{sg}\rangle=0.02$ for $\Delta_f/\Delta_g=16$). This fact explains the increase of the correlation coefficient C_{EM} with the filter size, shown in Table VI, when the subfilter variance is predicted inaccurately, as it is the case with SSM.

3. Sensitivity of the FDF approach to the assumed distribution

As mentioned before, the role of the specific assumption of a beta PDF for the FDF is also interesting. The idea of an assumed distribution to statistically describe one or several scalars for application to turbulent combustion has been studied by different authors,[51] although not in a LES context until more recently. Several choices have been made: a Gaussian profile,[52] a beta-PDF,[53] a density function composed of a uniform distribution with two delta functions at the limits 0 and 1,[54] or a clipped Gaussian.[55] All these density functions are based on the first two moments.

In order to investigate the effect of the assumed shape of the distribution, we construct the following simple two-moment-based composite PDF. We start with a uniform distribution between $\zeta_1>0$ and $\zeta_2<1$, which has the given values $\bar{Z}$ and Z^2_{sg} as mean and variance. These two conditions, along with the normalization one, constitute a system of three equations for three unknowns, namely, ζ_1, ζ_2 and the height of the FDF. However, the constraints $\zeta_1>0$ and $\zeta_2<1$ allow solution to the previous system of equations if and only if $Z^2_{sg}<\bar{Z}^2/3$ for $\bar{Z}<0.5$ or $Z^2_{sg}<(1-\bar{Z}^2)/3$ for $\bar{Z}>0.5$.

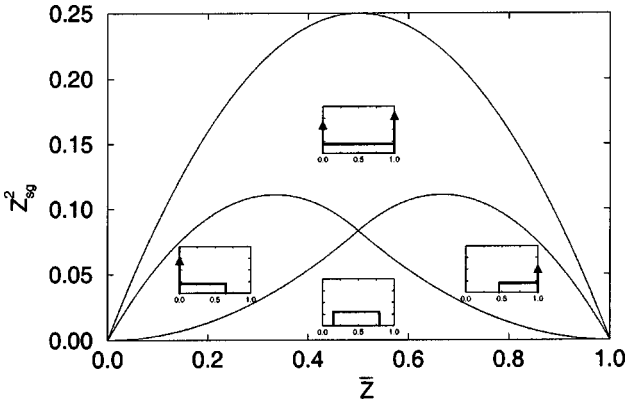

FIG. 31. Partition of the domain of definition of the composite PDF in four qualitatively different subdomains. The solid curves are the boundaries of the subregions and the shape of the corresponding PDF is shown as an inset. The case of the beta PDF is qualitatively the same.

This region in the domain of definition of the density function is the lower central zone in Fig. 31. For cases with $\bar{Z}<0.5$ and subgrid-scale variance greater than $\bar{Z}^2/3$, the left lower zone in that figure, we have to modify the presumed FDF such that it provides the required Z^2_{sg}. We do so by placing a δ function at $\zeta=0$, which is the usual solution found in the literature. The unknowns that define now the FDF are the magnitude of the δ function, the right limit ζ_2 of the uniform part and the height of this uniform zone. The equations are the same as before. Admissible solutions are now those that make $\zeta_2<1$, which imposes a new constraint in the unresolved variance, $Z^2_{sg}<\bar{Z}(2/3-\bar{Z})$. Similarly, we have the symmetric part, the right lower region in Fig. 31, with $\bar{Z}>0.5$ and a δ function at $\zeta=1$. Additionally, if Z^2_{sg} is larger than the level of fluctuations defined by the previous equations we are required to place one δ function at $\zeta=0$ and another at $\zeta=1$ besides the uniform distribution between 0 and 1, corresponding to the upper region in Fig. 31. This particular last case, only possible for high enough values of Z^2_{sg}, has already been used in the past.[54]

A first interesting observation is that a similar partition of the domain of definition of the FDF into four subregions is produced by the beta PDF. The boundary of each region is given by the conditions $a=1$ or $b=1$, a and b being the exponents of Eq. (65). If $a<1$, or equivalently $Z^2_{sg}>\bar{Z}^2(1-\bar{Z})/(1+\bar{Z})$ an (integrable) singularity appears at $\zeta=0$, which corresponds to the case of a δ function in the composite PDF. In the same way, a singularity occurs at $\zeta=1$ when $b<1$, which corresponds to the case $Z^2_{sg}>\bar{Z}(1-\bar{Z})^2/(2-\bar{Z})$.

The expected values of the various nonlinearities calculated using the composite PDF are very similar to the ones obtained using the beta PDF, the prediction of $\langle\omega(Z)_{sg}\rangle$ improving slightly at the edges of the jet, and in the polynomial case being indistinguishable from one another. These results are clear by considering $\langle P_Z\rangle(\zeta)$, which is shown in Fig. 27.

In terms of the pointwise behavior, the scatter plots give approximately the same correlation coefficients and they are indeed very much alike. Considering for instance the filter size $\Delta_f/\Delta_g=16$, the power function $Y(Z)$ yields C_{EM}

≈ 0.99 if the beta distribution is used, and $C_{EM} \approx 0.98$ is the composite distribution is utilized instead. In the case of $\omega(Z)$ with $Z_{st}=0.2$, $C_{EM} \approx 0.97$ in both cases.

These results indicate that the *particular shape* of the adopted FDF is *not* very important provided that it satisfies two conditions. First, the assumed FDF has to be used with the correct $\overline{Z}$ and Z_{sg}^2. Physically this means that the FDF takes into account intermittency (presence of pure unmixed fluids inside the filter cell) as well as small-scale diffusive mixing. The consequence of this condition is shown by the partition into four subregions with qualitatively different FDF shapes, as shown in Fig. 31. Second, the nonlinearity under consideration should not be very localized. If this second condition is met, there is compensation of errors in Eq. (63), for overestimation of the FDF in some parts of the interval $0 \leqslant \zeta \leqslant 1$ implies underestimation in others and, since the integral averages these deviations, some local inaccuracy in modeling the FDF is acceptable. Similar results have been found in the RANS context.[10]

4. Sensitivity of the FDF approach to the locality of the nonlinearity

Motivated by the preceding discussion, it is of interest to observe the behavior of the subgrid-scale model as the length scale ΔZ of the Arrhenius term (see Fig. 14) decreases. In typical combustion chemistry, the thickness of a nonpremixed flame is approximately proportional to a fractional power of the rate of local scalar dissipation,[4] χ_{st}. As χ_{st} decreases, so does the flame thickness in Z space (analogous to ΔZ here). Since χ_{st} is a random variable in a turbulent flow, the flame thickness varies from point to point and the subgrid-scale model must provide accurate predictions for instances in which the flame becomes very thin. We have seen that the reconstruction procedure can lose accuracy in such a situation. In a FDF context, the local estimate of the FDF in an interval ΔZ around Z_{st} becomes more important and, since a global averaging of error does not occur, the performance of an assumed FDF model is expected to deteriorate. This aspect was studied using the Burke–Schumann limit for $T(Z)$ and varying the ratio T_a/T_f to control ΔZ. Instead of the characteristic scale ΔZ given by Eq. (38) in Sec. V, we define it in this particular study by the interval between the points where the reaction rate drops to 10% of its maximum value. The characteristic length is then given by

$$\Delta Z = 1 - \frac{1}{1+(T_f/T_a)\ln 10}. \tag{70}$$

The limit $\Delta Z = 0$ was analyzed assuming a delta function at Z_{st}, which yields a direct comparison of actual values of $P_Z(Z_{st})$ against model predictions.

Figure 32 shows the correlation coefficients C_{EM} for both the beta and the composite distributions as a function of the scale ΔZ. The stoichiometric mixture fraction is $Z_{st}=0.2$ and the scatter plots of model against exact pointwise values were obtained at the location were $Z=Z_{st}$. The exact subfilter variance was used. Correlation coefficients are above 0.70 always, decreasing as ΔZ is reduced. For relatively large values of ΔZ, the composite PDF and the beta PDF do similarly, as reported before; the nonlinearity is sufficiently global so that the precise shape of the FDF is not crucial. As ΔZ decreases, the beta PDF represents slightly better the FDF, though there is not a big difference between the two FDF choices. For reacting flow problems in which ΔZ is small enough and a correlation greater than 70% is desired the estimated FDF has to be better than either a beta PDF or composite PDF.

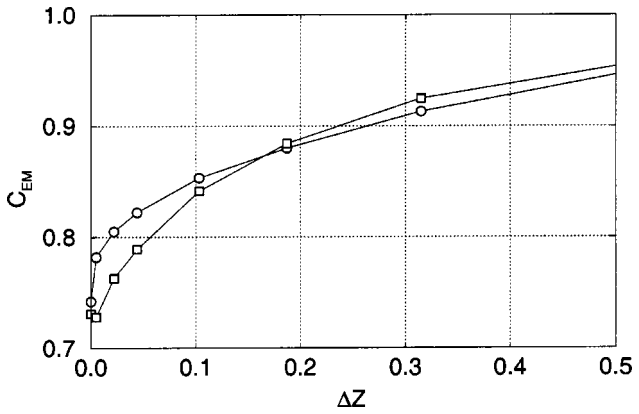

FIG. 32. Correlation coefficient between model predictions and exact values of $\overline{\omega}$ at the y location of the stoichiometric surface, $\langle \overline{Z} \rangle = Z_{st} = 0.2$, for different characteristic scales ΔZ: ○, beta PDF; □, composite PDF.

B. Combination of ARM and FDF approaches

To conclude the *a priori* analysis, and following logically from previous results, the ARM prediction of the subgrid-scale variance was utilized as the input to the FDF model, since the reconstruction is an approximation of a higher order than the scale similarity model at the low additional computational cost of one filtering operation. The ARM provides the spatial structure of the subgrid-scale variance field accurately, an input that is required in a presumed FDF approach.

Figure 33 shows the performance of the FDF–ARM model for the case of $Y(Z)=Z^4$. The correction in the poly-

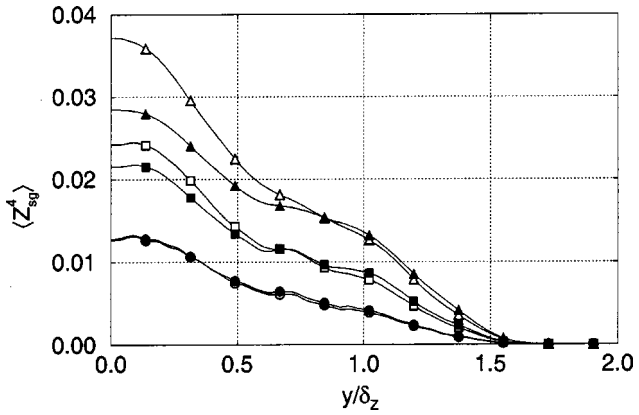

FIG. 33. Predictions of the SGS part of $Y(Z)=Z^4$. Hollow symbols correspond to exact values and solid symbols to FDF–ARM model predictions. Circles, squares, and triangles denote filter sizes of 4, 8, and 16, respectively.

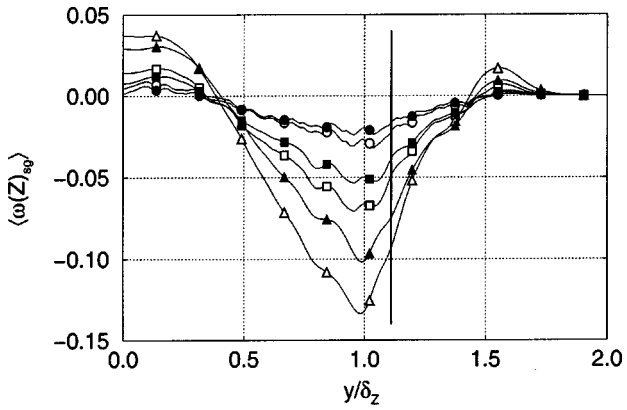

FIG. 34. Predictions of the SGS part of $\omega(Z)$. Hollow symbols correspond to exact values and solid symbols to FDF–ARM model predictions. Circles, squares, and triangles denote filter sizes of 4, 8, and 16, respectively. Vertical solid line indicates position of the stoichiometric surface, $\langle Z\rangle = 0.2$.

nomial case is clear, and the model prediction follows now the correct shape of the profile. The model prediction is slightly low, but this comes from the underprediction of the model coefficient due to low Reynolds number effects, as exposed previously. For high Péclet numbers, as c_0 approaches the asymptotic value, the agreement is expected to be better. Similarly, correlation coefficients are significantly increased, as shown in Table VI, going from 0.41 in the case of the scale similarity model to 0.88 if the ARM model is used. This is a consequence of the good spatial structure provided by ARM model. It has to be noted as well that the prediction of FDF–ARM model is similar to that of the ARM model alone for these polynomial cases.

Figure 34 correspond to the Arrhenius function $\omega(Z)$ for $Z_{st} = 0.2$. The improvement in the Arrhenius case is not very conspicuous for large filter sizes, because of the small sensitivity of this particular nonlinearity to the subgrid-scale variance, explained before. This behavior is observed in the expected values as well as in the pointwise results, with the correlation coefficient being very similar in the FDF and FDF–ARM models, 0.94 and 0.95, respectively. The improvement is more significant for the smaller filter sizes, when the influence of the subfilter variance is more notorious. The same conclusions can be drawn for the density function $\rho(Z)$.

A further extension of the presumed FDF model, not explored in this study, is to consider FDF models that involve more than two subgrid-scale moments.[56] ARM makes this feasible by providing the required moments with high accuracy, as the results from the analysis involving the polynomial terms prove.

The conclusion is that, for polynomial nonlinearities, the ARM model by itself provides very good predictions, of the order of or better than the FDF–ARM model, and the implementation of the ARM is very simple, specially for high Reynolds numbers when the model coefficient c_0 is just a constant. The same applies for the Arrhenius case and the density when the filter size is sufficiently small. For large filter sizes, the performance of FDF–ARM is similar to the standard FDF, despite the ARM prediction of the structure of the subgrid-scale variance field being better than the one provided by the scale similarity model; the reason is the small sensitivity of the Arrhenius and the density terms to the subgrid-scale variance once this latter quantity is above a certain threshold.

VII. CONCLUSIONS

Large-eddy simulation of combustion problems requires modeling of the subgrid-scale contribution, $\overline{f(Z)} - f(\overline{Z})$, that arises after filtering terms such as the reaction rate or the radiation terms, which involve strongly nonlinear functions, $f(Z)$, of a scalar, Z.

Reconstruction models, in which a intermediate field $Z_M(\mathbf{x},t)$ is estimated to calculate the subgrid-scale part, have been discussed here, with particular emphasis on approximate reconstruction using moments (ARM). The pure deconvolution procedure, Eq. (14), presents two drawbacks: first, the convergence of the Neumann series, Eq. (4), is too slow, and, second, deconvolution does not account for the unrecoverable subfilter scales. On the other hand, the scale similarity model, Eq. (18), only retains the leading order term of the reconstruction. The procedure of ARM, Eq. (20), combines purely mathematical deconvolution with additional physical input, namely, the expected value of the subfilter variance. In this work, a model spectrum applicable to the unresolved subgrid scales is used, which yields the model coefficient c_0 (see Fig. 3) as an explicit function of the filter size, Δ_f/L_Z, and the turbulent Péclet number, Pe_t. It has been shown that reconstruction provides a good spatial description of the subfilter variance and that ARM improves significantly the SSM prediction by adding only one additional filtering operation (see Fig. 10).

A priori studies of the ARM procedure have been carried out with a DNS database of a spatially evolving turbulent plane jet for filter sizes Δ_f/Δ_g of 4, 8, and 16, corresponding approximately to a LES with 30, 16, and 8 points per half-width of the jet at the downstream location of interest, 11 times the nozzle width. Here, Δ_f and Δ_g denote filter size and DNS grid spacing, respectively.

The results show that the averaged profiles of the subgrid-scale contribution of the variance, $\langle Z_{sg}^2\rangle$, agree well with the exact DNS data for the two smaller filter sizes, with errors less than 5%. The poorer response of the model for $\Delta_f/\Delta_g = 16$ is expected due to the large filter size, but still the error is less than 15% and it is due to the lack of isotropy of the subgrid scales for this low Reynolds number flow and the corresponding inapplicability of the model spectrum to all directions. In terms of the pointwise behavior, correlation coefficients between model predictions and exact values at the centerline of the jet are high, about 0.90 for the subgrid-scale part and above 0.95 for the total term.

Polynomial nonlinearities $Y(Z) = Z^n$ behave very similarly to the subfilter variance, and thus the results show that the subgrid-scale part can be correctly predicted with ARM. The density profile $\rho(Z) = 1/T(Z)$ has been considered for the typical case of methane-air combustion, with $Z_{st} = 0.055$. The errors in the prediction of the expected value are below 20% and correlation coefficients are of the order of

0.90. The Arrhenius term $\omega(Z)=\exp(-T_a/T(Z))$ has been analyzed. For a smooth case of $Z_{st}=0.2$ and $T_a/T_f=10$, the results show an error below 10% for the smallest filter size, while, for the largest filter size, these errors increase as the remainder in the Taylor's formula, Eq. (29), augments, until the order of 30%. The pointwise behavior is similar, with correlation coefficients between exact and predicted values of the unresolved part at the location $\langle\overline{Z}\rangle=Z_{st}$ above 0.90. However, as the characteristic scale ΔZ of the nonlinearity $\omega(Z)$ decreases, so does the performance of the ARM model, as expected from the rationale behind the approach.

A LES has been performed to obtain *a posteriori* results on a grid having spacing $\Delta_g^{\mathrm{LES}}=8\Delta_g^{\mathrm{DNS}}$. The closure in the momentum and scalar equations is done with a dynamic mixed procedure with filter size $\Delta_f=2\Delta_g^{\mathrm{LES}}$ and test filter size of $2\Delta_f$. The filter in the LES approximately corresponds to an *a priori* test with $\Delta_f=16\Delta_g^{\mathrm{DNS}}$. The main difference with respect to the *a priori* context is that the two physical quantities required by the ARM model, a velocity scale $K^{1/2}$ and a time scale Z_{rms}^2/χ, are approximated by resolved values $K_r^{1/2}$ (with a possible correction to estimate K) and $\overline{Z}_{\mathrm{rms}}^2/\chi_{\mathrm{sg}}$. It has been shown that the behavior of the model in the LES follows the same trends as in the *a priori* results, giving very accurate predictions of subgrid-scale contributions of polynomial functions and reasonable estimates of the stronger, more localized, Arrhenius nonlinearity. It has been explained as well that the LES must provide an accurate resolved field in order to calculate higher nonlinearities with the ARM method and, for this reason, a dynamic mixed model is preferred instead of a simpler dynamic Smagorinsky model.

A detailed analysis of the error involved in the ARM method has been presented. The first source of error lies in the assumption of isotropy of the subfilter scales and a particular scalar spectrum. This error is expected to decrease as the Reynolds number increases, and, besides, it has been shown that the sensitivity of the subgrid-scale variance to errors in the model coefficient is small, about 0.25. It is recognized that the spectral formulation is not always applicable (e.g., compressible cases or flows with inhomogeneities imposed on the subfilter scales, like in situations of strong shear or the presence of gravity) and alternatives are currently under investigation. The second source of error, associated with using the intermediate field Z_M to compute the subgrid part of the nonlinearity $f(Z)$, is estimated using a Taylor expansion of $f(Z)$. This analysis shows that the accuracy of the model depends on how large is the magnitude of the subfilter fluctuations compared to ΔZ, a particular scale for each nonlinearity $f(Z)$. Hence, the ratio $\lambda=(Z_{\mathrm{sg}}^2)^{1/2}/\Delta Z$ comes up as the controlling parameter of the model, a ratio that varies with the filter size as $\gamma^{1/3}$, where $\gamma=\Delta_f/2L_Z$. An expression to estimate ΔZ is given by Eq. (38), which can be used to choose the filter size of the LES in order to achieve the desired accuracy in the subgrid model. Values of λ for different nonlinearities and filter sizes are reported in Table V.

With the aim of comparing with the ARM model, the assumed filtered density function (FDF) approach has been considered in the *a priori* context. With respect to the polynomial terms, ARM is more accurate than FDF. Correlation coefficients for $Y(Z)=Z^4$ can be compared between Table II and Table VI. For instance, for the filter size of 16, ARM gives a correlation of 0.89 whereas FDF yields only 0.41. The combination FDF–ARM improves significantly the performance of the FDF approach because the polynomial nonlinearities have a high sensitivity to the subfilter variance field, and the results become similar to those of the ARM approach. With respect to the Arrhenius nonlinearity and density, it has been shown that for filter sizes such that $\lambda\ll 1$ the ARM and FDF predictions are comparable *if the subgrid-scale variance for the FDF is given by the ARM*. The scale similarity model does not provide sufficiently accurate estimates of the subfilter variance. This is shown through the correlation coefficients in Table VI. For higher levels of subgrid-scale fluctuations (larger filter sizes), the combination of FDF with ARM gives the best performance. ARM gives the correct spatial structure of the subgrid scalar contribution, while the FDF provides the correct magnitude.

ACKNOWLEDGMENTS

Partial support for the authors was provided by AFOSR through Grant No. F49620-96-1-0106 and Lawrence Livermore National Laboratory through the Student Employee Graduate Research Fellowship Program. This work was supported in part by a grant of HPC time at the Naval Oceanographic Office Department of Defense Major Shared Resource Center.

APPENDIX A: LOCAL ANALYSIS OF THE FILTER

Consider a particular filter cell $\Omega_f(\mathbf{x})$ at a fixed point $\mathbf{x}$, which is the domain of the mapping $\mathbf{r}\rightarrow G(\mathbf{x},\mathbf{r})$. If we assume a positive filter, then we can define an inner product by

$$(\phi,\psi)=\int_{\Omega_f} G(\mathbf{x},\mathbf{r})\,\phi(\mathbf{r})\,\psi^*(\mathbf{r})\,d\mathbf{r} \tag{A1}$$

in the linear space of square-integrable functions defined over $\Omega_f(\mathbf{x})$.[57] The asterisk as superscript indicates complex conjugate. We assume that the integral of $|\phi|^2$ over Ω_f is finite for any flow variable $\phi(\mathbf{r})$ at any instant of time t. The assumption of positive filter, i.e., $G(\mathbf{x},\mathbf{r})\geqslant 0$ (excluding the zero function), physically, is a necessary condition if we desire to maintain positiveness of the filtered quantities of positive variables, like temperature, density or pressure. This inner product induces the L^2 norm

$$\|\phi\|=(\phi,\phi)^{1/2}. \tag{A2}$$

Consider a specific nodal value, $\overline{\phi}(\mathbf{x})$, on the LES grid. We take $\overline{\phi}(\mathbf{x})$ to be a constant value inside the associated filter cell $\Omega_f(\mathbf{x})$ to define a *local subfilter field* by

$$\phi_{l\mathrm{sg}}(\mathbf{r})=\phi(\mathbf{r})-\overline{\phi}(\mathbf{x}),\quad \mathbf{r}\in\Omega_f(\mathbf{x})\quad \text{for a fixed } \mathbf{x}. \tag{A3}$$

Note that this is different from the usual one, $\phi_{\mathrm{sg}}(\mathbf{r})=\phi(\mathbf{r})-\overline{\phi}(\mathbf{r})$. It is straightforward to show that the L^2 norm of $\phi_{l\mathrm{sg}}$ is just the square root of the subgrid-scale variance of ϕ at the point $\mathbf{x}$,

TABLE VII. ARM model for different filters in the limit of high Péclet number under isotropic conditions: subfilter variance $\langle Z_{sg}^2 \rangle$ in the first column, followed by the recoverable part of it, model coefficient c_0 and sensitivity Γ of the modeled variance to c_0.

Filter	Transfer function	a	b	c_0	Γ
Top-hat	$\sin\xi/\xi$	1.44	0.52	4.09	0.27
Gaussian	$\exp(-\xi^2/6)$	1.41	0.50	4.35	0.24
Top-hat and cutoff	$(\sin\xi/\xi)H(\pi-\xi)$	1.44	0.52	4.85	0.23
Gaussian and cutoff	$\exp(-\xi^2/6)H(\pi-\xi)$	1.41	0.50	4.49	0.24
Mid-point and cutoff	$\frac{1}{2}(1+\cos\xi)H(\pi-\xi)$	1.64	0.57	4.72	0.23
Simpson and cutoff	$\frac{1}{3}(2+\cos\xi)H(\pi-\xi)$	1.40	0.50	4.31	0.24

$$\|\phi_{lsg}\| = (\phi_{sg}^2)^{1/2}. \tag{A4}$$

This result is the motivation to have used the L^2 norm, for the ARM model is designed to provide accurately the pointwise instantaneous value of the subgrid-scale variance in a LES, and this quantity is *identical* to the L^2 norm of the local subfilter field in $\Omega_f(\mathbf{x})$.

It is convenient to take the expected value of the previous pointwise quantity, which leads to the inequality

$$\langle \|\phi_{lsg}\| \rangle \leqslant \langle \phi_{sg}^2 \rangle^{1/2}. \tag{A5}$$

This is proved considering the probability density functions $p_g(G)$ and $p_h(H)$ of the random variables $g=\phi_{sg}^2$ and $h=g^{1/2}$, respectively. Then, basic probability theory shows that $p_h(H)=2Hp_g(H)$, where $H\leqslant 0.25^2$ because of Eq. (A6), having then $\langle h\rangle \leqslant \langle g\rangle$. The last step is $\langle g\rangle \leqslant \langle g\rangle^{1/2}$ because $g\leqslant 1$, obtaining the desired result.

A few useful relations are now derived. First, it is easy to show that the inequality

$$0 \leqslant \phi_{sg}^2 \leqslant \overline{\phi}(1-\overline{\phi}) \tag{A6}$$

always holds for a field $\phi(\mathbf{x})$ satisfying $0\leqslant\phi\leqslant 1$, as it is the case for the mixture fraction Z or the species mass fractions Y_i. In general, all we require is boundedness, for then we can just think in terms of a normalized field; for instance, the temperature is going to be bounded from above by the adiabatic flame temperature, so T/T_f remains between 0 and 1. The first part of the above inequality holds for any positive filter, since the Cauchy–Schwarz inequality, along with the normalization condition of $G(\mathbf{x},\mathbf{r})$, yields

$$|\overline{\phi}|^2 \leqslant \overline{\phi^2} \tag{A7}$$

and the positiveness of the filter ensures $\overline{\phi}>0$ if $\phi>0$. The second part follows because

$$0\leqslant\phi\leqslant 1 \Rightarrow \phi^2 \leqslant \phi \Rightarrow \overline{\phi^2} \leqslant \overline{\phi} \Rightarrow \overline{\phi^2}-\overline{\phi}^2 \leqslant \overline{\phi}-\overline{\phi}^2, \tag{A8}$$

where the positiveness of $G(\mathbf{x},\mathbf{r})$ is required again in the second implication. Hence, an upper bound to the subgrid-scale variance is 0.25, the maximum of $\overline{\phi}(1-\overline{\phi})$.

Following the same reasoning, i.e., $\phi^n\leqslant\phi^{n-1}\leqslant\phi$, Eq. (A6) can be generalized to higher order moments, obtaining

$$\phi_{sg}^n \leqslant \phi_{sg}^{n-1} + \overline{\phi}^{n-1}(1-\overline{\phi}) \leqslant \overline{\phi}(1-\overline{\phi}^{n-1}). \tag{A9}$$

This relation can be used as a constraint in any presumed FDF model that depends on n moments.

Finally, we consider the sign of the subgrid scale part of a nonlinearity $f(\phi)$. If this function has globally nonnegative curvature, $f''(\phi)\geqslant 0$, then the inequality

$$f(\phi) \geqslant f(\phi_0) + f'(\phi_0)(\phi-\phi_0) \tag{A10}$$

holds for any ϕ and ϕ_0. If ϕ_0 is considered constant and equal to $\overline{\phi}$ and this equation is filtered, the order relation is maintained by the positive filter to yield

$$f''(\phi)\geqslant 0, \quad \forall\phi \Rightarrow \overline{f(\phi)} - f(\overline{\phi}) \geqslant 0.$$

Examples considered in this paper that fall into this case are the polynomials and the density profile of Fig. 12. Similarly, it can be proved that if $f(\phi)$ is convex, then the subgrid scale part is negative; the typical example would be the temperature as a function of the mixture fraction. There are nonlinearities $f(\phi)$ that are convex in some regions and concave in others, for instance the Arrhenius term, displayed in Fig. 14, or the radiation loses proportional to the fourth power of the temperature in the optically thin regime; their subfilter part can be either positive or negative.

APPENDIX B: RESULTS FOR OTHER FILTERS

For completeness, we consider here various filters in addition to the top-hat and calculate some results presented previously for the top-hat. Isotropic turbulence at high Péclet numbers is always assumed, in order to work with the spectral formulation. The data are gathered in Table VII. First, the amount of fluctuation energy represented by the subfilter scales,

$$a = \langle Z_{sg}^2 \rangle / (Z_{rms}^2 C_c \gamma^{2/3}) \tag{B1}$$

given by Eq. (12), is calculated, along with the recoverable part of it, $\langle Z_{sg}^2 \rangle_r$, given by that same integral in the interval $[0,\pi]$,

$$b = \langle Z_{sg}^2 \rangle_r / \langle Z_{sg}^2 \rangle. \tag{B2}$$

Recall that $\gamma=\Delta_f/2L_Z$ is the normalized filter width. Second, the ARM model coefficient c_0, Eq. (23) and Eq. (44), and the sensitivity Γ, Eq. (27), are computed.

The kernel for the *Gaussian filter*[41] is

$$G(r) = (6/\pi\Delta_f^2)^{1/2} \exp(-6r^2/\Delta_f^2). \tag{B3}$$

The effect of the grid cutoff at Δ_f (which means a grid spacing $\Delta_g=\Delta_f/2$) is expressed by the spectral low-pass filter $H(\pi-\xi)$, where $H(\xi)$ is the Heaviside function and ξ

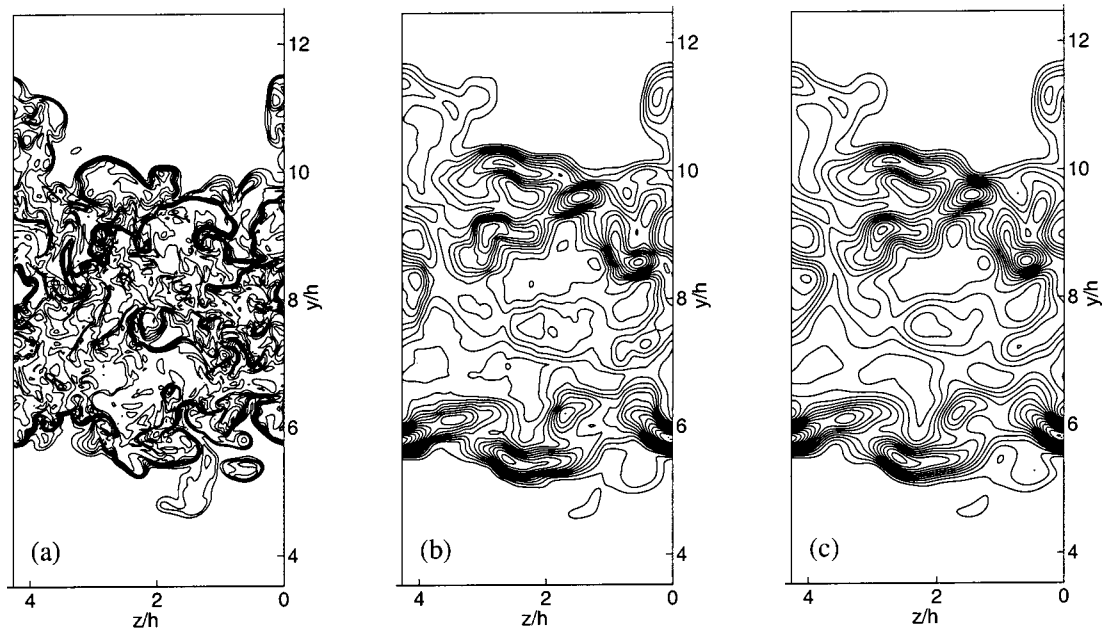

FIG. 35. Effect of sampling the scalar field in the *a priori* results. From left to right, contour plots at the plane $x/h=11.0$: (a) Z, (b) Z_{sg}^2 with a top-hat filter of $\Delta_f/\Delta_g=16$, and (c) Z_{sg}^2 with a top-hat filter of $\Delta_f/\Delta_g=16$ plus sampling at $\Delta_f/2$.

$=\gamma\kappa L_Z$. The last two cases represent the usual discrete version of the top-hat, depending on the integration rule employed. The *midpoint filter* is given by

$$G(r)=1/4(\delta(r+\Delta_f/2)+2\delta(r)+\delta(r-\Delta_f/2)), \tag{B4}$$

and the *Simpson filter* is expressed by

$$G(r)=1/6(\delta(r+\Delta_f/2)+4\delta(r)+\delta(r-\Delta_f/2)). \tag{B5}$$

It is worth noticing that these last two discrete filters, represented in a continuous fashion with the aid of the delta function, do not include a spectral cutoff, and this has to be additionally imposed to represent the effect of the grid.

From the numbers of Table VII it is clear that there is little difference among the various filters. Reconstruction allows to recover about 50% of the subfilter energy for every filter, as shown by the parameter b. The model coefficient does not vary considerably. The mean value of c_0 is 4.5 and all the filters have a model coefficient in a range of 4.5 ± 0.4. Note that although the spectral cutoff means less than 1% of the subfilter energy (a is invariant in the first two decimals), the model coefficient feels it more because it is coupled with the smallest resolved scales, Eq. (20).

APPENDIX C: EFFECT OF THE MESH ON THE *A PRIORI* RESULTS

The filtering operation is applied to the scalar field using the grid from the DNS (DNS grid), which is much finer than the grid one would use performing a LES (LES grid). It is difficult to evaluate the consequence of a sharp spectral cutoff at the wave number $2\pi/\Delta_f$ associated with the LES grid, defined by $\Delta_g=\Delta_f/2$, because it is complicated to perform a Fourier transform of Z without homogeneity in the x direction. One alternative would be to sample the filtered field onto the LES grid and then go back to the DNS grid if desired using an interpolation. The aliasing error in the sampling, if done after filtering, involves less than 1% of the subgrid-scale energy, corresponding to the lobes of the top-hat filter transfer function for $\kappa>2\pi/\Delta_f$. This estimate is obtained using the same kind of analysis that yields Eq. (12). The energy in excess in the DNS grid is

$$(Z_{\mathrm{rms}}^2 C_c\gamma^{2/3})\int_{\pi}^{\infty}(\sin\xi/\xi)^2\xi^{-5/3}\,d\xi$$

$$=0.0074(Z_{\mathrm{rms}}^2 C_c\gamma^{2/3}), \tag{C1}$$

less than one per cent of the result in Eq. (12).

As a consequence, results were practically the same between using the DNS grid or the LES grid. The pointwise behavior is also similar, as shown in Fig. 35, where differences of the field Z_{sg}^2 in the DNS grid and the LES grid are very small.

[1] *Turbulent Reacting Flows*, edited by P. A. Libby and F. A. Williams (Springer-Verlag, New York, 1980).
[2] F. A. Williams, *Combustion Theory* (Addison Wesley, New York, 1985).
[3] *Turbulent Reacting Flows*, edited by P. A. Libby and F. A. Williams (Academic, Philadelphia, 1994).
[4] N. Peters, *Turbulent Combustion* (Cambridge University Press, Cambridge, 2000).
[5] T. Poinsot and D. Veynante, *Theoretical and Numerical Combustion* (Edwards, New York, 2001).
[6] E. E. O'Brien, "The probability density function (pdf) approach to reacting turbulent flows," in *Turbulent Reacting Flows*, edited by P. A. Libby and F. A. Williams (Springer-Verlag, New York, 1980), pp. 185–218.
[7] S. B. Pope, "PDF methods for turbulent reactive flows," Prog. Energy Combust. Sci. **11**, 119 (1985).
[8] R. P. Lindstedt, S. A. Louloudi, and E. M. Váos, "Joint scalar probability density function modeling of pollutant formation in piloted turbulent jet diffusion flames with comprehensive chemistry," Proc. Combust. Inst. **28**, 149 (2000).
[9] R. W. Bilger, "Turbulent jet diffusion flames," Prog. Energy Combust. Sci. **1**, 87 (1976).

[10]R. W. Bilger, ''Turbulent flows with nonpremixed reactants,'' in *Turbulent Reacting Flows*, edited by P. A. Libby and F. A. Williams (Springer-Verlag, New York, 1980), pp. 65–113.
[11]F. A. Williams, ''Recent advances in theoretical descriptions of turbulent diffusion flames,'' in *Turbulent Mixing in Reactive and Nonreactive Flows*, edited by S. N. Murthy (Plenum, New York, 1975), pp. 189–208.
[12]N. Peters, ''Laminar diffusion flamelet models in nonpremixed turbulent combustion,'' Prog. Energy Combust. Sci. **10**, 319 (1984).
[13]N. Peters, ''Laminar flamelet concepts in turbulent combustion,'' *Twenty-First Symposium (Intl.) on Combustion* (The Combustion Institute, Pittsburgh, 1986), pp. 1231–1250.
[14]K. N. C. Bray and N. Peters, ''Laminar flamelets in turbulent flames,'' in *Turbulent Reacting Flows*, edited by P. A. Libby and F. A. Williams (Academic, New York, 1994), pp. 63–113.
[15]R. W. Bilger, ''Conditional moment closure for turbulent reacting flow,'' Phys. Fluids A **5**, 436 (1993).
[16]A. Y. Klimenko, ''Multicomponent diffusion of various admixtures in turbulent flows,'' Fluid Dyn. **25**, 327 (1990).
[17]A. Y. Klimenko, ''On the relation between the consitional moment closure and unsteady flamelets,'' Combust. Theory Model. **5**, 275 (2001).
[18]A. R. Kerstein, ''A linear-eddy model of turbulent scalar transport and mixing,'' Combust. Sci. Technol. **60**, 391 (1988).
[19]P. A. McMurtry, S. Menon, and A. R. Kerstein, ''Linear eddy modeling of turbulent combustion,'' Energy Fuels **7**, 817 (1993).
[20]W. W. Kim, S. Menon, and H. C. Mongia, ''Large-eddy simulation of a gas turbine combustor flow,'' Combust. Sci. Technol. **143**, 25 (1999).
[21]F. Gao and E. E. O'Brien, ''A large-eddy simulation scheme for turbulent reacting flows,'' Phys. Fluids A **5**, 1282 (1993).
[22]P. J. Colucci, F. A. Jaberi, P. Givi, and S. B. Pope, ''Filtered density function for large eddy simulation of turbulent reacting flows,'' Phys. Fluids **10**, 499 (1998).
[23]C. K. Madnia and P. Givi, ''Direct numerical simulation and large eddy simulation of reacting homogeneous turbulence,'' in *Large Eddy Simulation of Complex Engineering and Geophysical Flows*, edited by B. Galperin and S. A. Orszag (Cambridge University Press, Cambridge, 1993).
[24]A. W. Cook and J. J. Riley, ''A subgrid model for equilibrium chemistry in turbulent flows,'' Phys. Fluids **6**, 2868 (1994).
[25]A. W. Cook, ''Determination of the constant coefficient in scale similarity models of turbulence,'' Phys. Fluids **9**, 1485 (1997).
[26]C. D. Pierce and P. Moin, ''A dynamic model for subgrid-scale variance and dissipation rate of a conserved scalar,'' Phys. Fluids **10**, 3041 (1998).
[27]A. W. Cook, J. J. Riley, and G. Kosály, ''A laminar flamelet approach to subgrid-scale chemistry in turbulent flows,'' Combust. Flame **109**, 332 (1997).
[28]A. W. Cook and J. J. Riley, ''Subgrid-scale modeling for turbulent reacting flows,'' Combust. Flame **112**, 593 (1998).
[29]J. Jiménez, A. Liñán, M. M. Rogers, and F. J. Higuera, ''*A priori* testing of subgrid models for chemically reacting non-premixed turbulent shear flows,'' J. Fluid Mech. **349**, 149 (1997).
[30]C. Wall, B. J. Boersma, and P. Moin, ''An evaluation of the assumed beta probability density function subgrid-scale model for large eddy simulation of nonpremixed, turbulent combustion with heat release,'' Phys. Fluids **12**, 2522 (2000).
[31]H. Pitsch and H. Steiner, ''Large-eddy simulation of a turbulent piloted methane/air diffusion flame (Sandia flame D),'' Phys. Fluids **12**, 2541 (2000).
[32]C. Pantano and S. Sarkar, ''A subgrid model for nonlinear functions of a scalar,'' Phys. Fluids **13**, 3803 (2001).
[33]A. Leonard, ''Energy cascade in large-eddy simulations of turbulent fluid flows,'' Adv. Geophys. **18**, 237 (1974).
[34]J. Bardina, J. H. Ferziger, and W. C. Reynolds, ''Improved subgrid models for large eddy simulation,'' AIAA Paper 80-1357, 1980.
[35]J. A. Domaradzki and E. M. Saiki, ''A subgrid-scale model based on the estimation of unresolved scales of turbulence,'' Phys. Fluids **9**, 2148 (1997).
[36]J. A. Domaradzki and K. Loh, ''The subgrid-scale estimation model in physical space representation,'' Phys. Fluids **11**, 2330 (1999).
[37]B. J. Geurts, ''Inverse modeling for large-eddy simulation,'' Phys. Fluids **9**, 3585 (1997).
[38]S. Stolz and N. A. Adams, ''An approximate deconvolution procedure for large-eddy simulation,'' Phys. Fluids **11**, 1699 (1999).
[39]A. W. Naylor and G. R. Sell, *Linear Operator Theory in Engineering and Science* (Springer-Verlag, New York, 1982).
[40]P. Linz, *Theoretical Numerical Analysis* (Dover, New York, 1979).
[41]S. B. Pope, *Turbulent Flows* (Cambridge University Press, Cambridge, 2000).
[42]H. Tennekes and J. L. Lumley, *A First Course in Turbulence* (MIT Press, Cambridge, MA, 1972).
[43]K. R. Sreenivasan, ''The passive scalar spectrum and the Obukhov–Corrsin constant,'' Phys. Fluids **8**, 189 (1996).
[44]L. Mydlarski and Z. Warhaft, ''Passive scalar statistics in high-Péclet-number grid turbulence,'' J. Fluid Mech. **358**, 135 (1998).
[45]J. W. Deardoff, ''On the magnitude of the subgrid scale eddy-viscosity coefficient,'' J. Comput. Phys. **7**, 120 (1971).
[46]S. A. Stanley, S. Sarkar, and J. P. Mellado, ''A study of the flow-field evolution and mixing in a planar turbulent jet using direct numerical simulation,'' J. Fluid Mech. **450**, 377 (2002).
[47]F. J. Higuera and R. D. Moser, ''Effect of chemical heat release in a temporally evolving mixing layer,'' CTR Report, 1994, pp. 19–40.
[48]C. Le Ribault, S. Sarkar, and S. A. Stanley, ''Large eddy simulation of a plane jet,'' Phys. Fluids **11**, 3069 (1999).
[49]C. Le Ribault, S. Sarkar, and S. A. Stanley, ''Large eddy simulation of evolution of a passive scalar in plane jet,'' AIAA J. **39**, 1509 (2001).
[50]S. B. Pope, ''Computations of turbulent combustion: Progress and challenges,'' *Twenty-Third Symposium (Intl.) on Combustion* (The Combustion Institute, Pittsburgh, 1990), pp. 591–612.
[51]S. B. Pope, ''The statistical theory of turbulent flames,'' Philos. Trans. R. Soc. London, Ser. A **291**, 529 (1979).
[52]W. R. Hawthorne, D. S. Wedell, and H. C. Hottel, ''Mixing and combustion in turbulent gas jets,'' *Third Symposium (Intl.) on Combustion* (Williams and Wilkins, Baltimore, 1949), pp. 266–288.
[53]J. M. Richardson, H. C. Howard, and R. W. Smith, ''The relation between sampling-tube measurements and concentration fluctuations in a turbulent gas jet,'' *Fourth Symposium (Intl.) on Combustion* (Williams and Wilkins, Baltimore, 1953), pp. 814–817.
[54]W. B. Bush and F. E. Fendell, ''On diffusion flames in turbulent shear flows,'' ACTA Aeronaut. Astronaut. Sinica **1**, 645 (1974).
[55]F. C. Lockwood and A. S. Naguib, ''The prediction of the fluctuations in the properties of free, round-jet, turbulent, diffusion flames,'' Combust. Flame **24**, 109 (1975).
[56]E. Effelsberg and N. Peters, ''A composite model for the conserved scalar PDF,'' Combust. Flame **50**, 351 (1983).
[57]B. Vreman, B. Geurts, and H. Kuerten, ''Realizability conditions for the turbulent stress tensor in large-eddy simulation,'' J. Fluid Mech. **278**, 351 (1994).